HHS Public Access

Author manuscript

J Am Chem Soc. Author manuscript; available in PMC 2018 December 06.

Published in final edited form as:

J Am Chem Soc. 2017 December 06; 139(48): 17313–17326. doi:10.1021/jacs.7b06246.

Equilibrating (L)Fe^{III}–OOAc and (L)Fe^{V}(O) Species in Hydrocarbon Oxidations by Bio-Inspired Nonheme Iron Catalysts using H_2O_2 and AcOH

Williamson N. Oloo[a], **Rahul Banerjee**[b], **John D. Lipscomb**[b,*], and **Lawrence Que Jr.**[a,*]

[a]Department of Chemistry and Center for Metals in Biocatalysis, University of Minnesota, Minneapolis, MN 55455 (United States)

[b]Department of Biochemistry, Molecular Biology, and Biophysics and Center for Metals in Biocatalysis, University of Minnesota, Minneapolis, MN 55455 (United States)

Abstract

Inspired by the remarkable chemistry of the family of Rieske oxygenase enzymes, nonheme iron complexes of tetradentate N4 ligands have been developed to catalyze hydrocarbon oxidation reactions using H_2O_2 in the presence of added carboxylic acids. The observation that the stereo- and enantioselectivity of the oxidation products can be modulated by the electronic and steric properties of the acid implicates an oxidizing species that incorporates the carboxylate moiety. Frozen solutions of these catalytic mixtures generally afford two $S = ½$ intermediates, a highly anisotropic g2.7 subset (g_{max} = 2.58 to 2.78 and Δg = 0.85 – 1.2) that we assign to an Fe^{III}–OOAc species and the less anisotropic g2.07 subset (g = 2.07, 2.01, and 1.96 and $\Delta g \sim 0.11$) we associate with an Fe^{V}(O)(OAc) species. Kinetic studies on the reactions of iron complexes supported by the TPA (tris(pyridyl-2-methyl)amine) ligand family with H_2O_2/AcOH or AcOOH at −40 °C reveal the formation of a visible chromophore at 460 nm, which persists in a steady state phase and then decays exponentially upon depletion of the peroxo oxidant with a rate constant that is substrate independent. Remarkably, the duration of this steady state phase can be modulated by the nature of the substrate and its concentration, which is a rarely observed phenomenon. A numerical simulation of this behavior as a function of substrate type and concentration affords a kinetic model in which the two intermediates exist in a dynamic equilibrium that is modulated by the electronic properties of the supporting ligands. This notion is supported by EPR studies of the reaction mixtures. Importantly, these studies unambiguously show that the g2.07 species, and not the g2.7 species, is responsible for substrate oxidation in the (L)Fe^{II}/H_2O_2/AcOH catalytic system. Instead the g2.7 species appears to be off-pathway and serves as a reservoir for the g2.07 species. These findings will be helpful not only for the design of regio- and stereo-specific nonheme iron oxidation catalysts but also for providing insight into the mechanisms of the remarkably versatile oxidants formed by nature's most potent oxygenases.

*Corresponding Authors: larryque@umn.edu. lipsc001@umn.edu.

Notes

The authors declare no competing financial interest.

Supporting Information

The Supporting Information is available free of charge on the ACS Publications website at DOI: xxxxxx. The supporting information provides further details on the UV–vis and EPR experiments for the generation and reactivity of **2**, **3** and **5**.

Graphical abstract

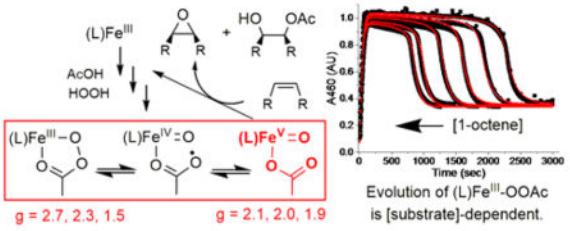

INTRODUCTION

The oxidation of hydrocarbons is a process of significant biological and industrial importance. Our approach to designing new synthetic catalysts for oxidative hydrocarbon transformations is inspired by the many iron-dependent oxygenases that have evolved in biological systems for the stereoselective oxidation of C–H and C=C bonds.[1–3] Among these biological catalysts, a particularly broad and versatile class activates dioxygen at an iron center ligated by a common 2-histidine-1-carboxylate facial triad motif.[3–6] One of the more intriguing members of this class is the Rieske oxygenase family of enzymes, which requires two electrons from NADH to activate dioxygen and carry out a wide array of important transformations, including C–H and C=C bond oxygenation, *O*- and *N*-demethylation, and C–C bond formation.[5, 7] For naphthalene 1,2-dioxygenase and carbazole 1,9a-dioxygenase, O_2 adducts of the respective enzyme-substrate complexes have been trapped in crystals and found to possess a dioxygen unit that is side-on bound to the iron center and in close proximity to the target C=C bond of the bound substrate.[8, 9] This O_2 adduct is speculated to correspond to the (hydro)peroxoiron(III) intermediate observed in the “peroxide shunt” reaction of fully oxidized benzoate 1,2-dioxygenase, which is capable of producing one turnover of the expected *cis*-diol product.[10] Additional studies on the reaction of benzoate 1,2-dioxygenase with dioxygen suggest that O_2 binds to the mononuclear Fe^{II} to form an Fe^{III}-superoxo species that attacks the substrate.[11] This transient species is stabilized by a nearly simultaneous electron transfer from the Rieske cluster to yield an Fe^{III}-peroxo species. Whether these peroxoiron(III) intermediates directly yield the oxidation products, or first undergo O–O bond cleavage to generate intermediate (L)Fe^{V}(O) oxidizing species is currently not clear. This puzzle has motivated chemists to design and study synthetic model complexes that resemble the active site species and/or duplicate function,[12–18] which can provide fundamental insights into the oxidative chemistry, in addition to the discovery of practical systems for the synthesis of organic compounds.

Inspired by the broad range of oxidative reactivities exhibited by the Rieske enzyme family,[5] particularly with respect to C–H bond cleavage and C=C bond oxidation, we and others have described a family of synthetic mono-iron catalysts supported by tetradentate N4 ligands that can mediate C–H bond hydroxylation and C=C bond epoxidation and *cis*-dihydroxylation using H_2O_2 as the oxidant.[12–18] In these systems, the H_2O_2 serves as a convenient substitute for the $O_2/2e^-/2H^+$ combination utilized by the oxygenases.[10, 19] Analogous to the biological reactions, the synthetic Fe(L)/H_2O_2 reaction mixtures afford Fe^{III}–OOH intermediates, which have been trapped and characterized at −40 °C for a

number of these bio-inspired catalysts.[17, 20–28] Initially, the observed incorporation of ^{18}O from added $H_2{}^{18}O$ into the alkane or olefin oxidation products led us to propose a "water-assisted mechanism",[17, 22, 23] in which an iron-bound water ligand promotes the heterolytic cleavage of the O–O bond of the peroxoiron(III) intermediate to generate an $Fe^{V}(O)(OH)$ oxidant, analogous to that proposed for the Rieske oxygenases.[29, 30] This idea was corroborated by Costas and co-workers in their observation of suitably labelled $(L)Fe^{V}(O)(OH)$ ions by cold spray ionization mass spectrometry when the ions were generated in the presence of $H_2{}^{18}O_2$ or $H_2{}^{18}O$.[31, 32] In further support, recent kinetic studies revealed an H_2O/D_2O isotope effect in the decay of the Fe^{III}–OOH intermediate as well as in the formation of the diol and epoxide products of 1-octene oxidation.[28]

The efficiency and selectivity of these iron catalysts have been further enhanced by replacing water with carboxylic acids.[33, 34] This has resulted in the development of synthetically useful transformations where specific C–H bonds in polyfunctional organic molecules can be oxidized with surprisingly high selectivity.[13, 35–38] The carboxylic acid additive has also led to the development of highly enantioselective olefin epoxidation reactions,[16, 18, 39–42] for which the % enantiomeric excess can be modulated by the steric bulk of the carboxylic acid[40, 43] and the electronic properties of the supporting ligand.[41]

Mechanistic studies aimed at elucidating the "magic" elicited by the carboxylic acid additive have been unexpectedly complicated. EPR studies at cryogenic temperatures on reaction mixtures of the Fe(L) catalysts with H_2O_2/RC(O)OH or peracids have revealed the formation of transient $S = ½$ intermediates that have stimulated significant discussion regarding the oxidation states of the iron centers. These $S = ½$ species can be broadly classified into two categories on the basis of their EPR anisotropy (Table 1): (i) a highly anisotropic subset (hereafter referred to as g2.7 species) with g_{max} values ranging from 2.58 to 2.78 ($\Delta g = 0.85 – 1.2$), and (ii) a much less anisotropic subset (referred to as g2.07 species) with invariant g-values of 2.07, 2.01, and 1.96 ($\Delta g \sim 0.11$).[40, 44–50] The structural assignments and reactivity patterns of these two subsets of intermediates have, however, remained unclear, as there are contradictory interpretations regarding the nature of the iron center in the literature.[17, 49, 51–54] For example, the g2.7 species supported by the TPA ligand (Scheme 1) has been assigned based on EPR evidence alone by Talsi and co-workers as an $Fe^{V}(O)(OAc)$ species,[44, 45, 49] while the analogous g2.7 intermediate supported by TPA* has been identified by some of us as an Fe^{III}–κ^2-OOAc species based on a more comprehensive spectroscopic analysis.[26] Additionally, the g2.07 species supported by the TPA* and PDP* ligands, first observed by Talsi, have been assigned as $Fe^{IV}(O)(^{\bullet}OAc)$ species, where the oxidizing equivalents are distributed between the ligand and the iron center.[51, 52] However, detailed EPR studies by Costas and co-workers on a related g2.07 species have argued against the $Fe^{IV}(O)(^{\bullet}OAc)$ characterization and instead favored an $Fe^{V}(O)$ electronic structure for which the oxidizing equivalents are predominantly located on the iron center.[54] This contradiction extends to the reactivity patterns, as the g2.7 species supported by the TPA ligand was reported to epoxidize cyclohexene at a rate dependent on olefin concentration,[44, 49] whereas the decay rate of the related g2.7 species supported by TPA* was unaffected by the nature and concentrations of various olefins.[50] More significantly, the connection between the g2.7 and g2.07 species has not yet been

established, even though these seemingly related subsets of intermediates are generated under comparable reaction conditions.

Herein, we describe detailed kinetic studies that demonstrate the presence of an equilibrium between the g2.7 and the g2.07 species. Accompanied by a more comprehensive spectroscopic analysis, this work also enables a more definitive assignment of the nature of the two novel intermediates. Insight into the role of each intermediate in hydrocarbon oxidation reactions by the (L)Fe/H_2O_2/RC(O)OH catalytic systems, where L = tetradentate N4 ligand is also provided. Overall, these studies provide clarity to current contradictions that surround the structural assignment and reactivity patterns of the g2.7 and g2.07 intermediate classes.

EXPERIMENTAL SECTION

Materials

All reagents and solvents used were of commercially available quality, unless otherwise stated. Solvents were purchased from Acros and Sigma-Aldrich and used without further purification. Peracetic acid was purchased from Aldrich as a 32 wt % solution in acetic acid containing less than 6 % H_2O_2, while cyclohexane peroxycarboxylic acid (CPCA) was prepared according to published procedures.[55] Compounds **1a** and **1a*** were prepared as previously described.[23, 50]

Physical Methods

UV-visible spectra were recorded on a Hewlett-Packard 8453A diode array spectrometer equipped with a cryostat from Unisoku Scientific Instruments, Osaka, Japan. X-band EPR spectra were recorded on a Bruker Elexsys E-500 spectrometer equipped with an Oxford ESR 910 liquid helium cryostat and an Oxford temperature controller. The quantification of the signals was relative to a Cu-EDTA spin standard. The SpinCount software for EPR analysis was provided by Dr. Michael P. Hendrich of Carnegie Mellon University.

Product analyses were performed on a Perkin-Elmer Sigma 3 gas chromatography (AT-1701 column, 30 m) and a flame-ionization detector. GC mass spectral analyses were performed on a HP 5898 GC (DB-5 column, 60 m) with a Finnigan MAT 95 mass detector or a HP 6890 GC (HP-5 column, 30 m) with an Agilent 5973 mass detector. NH_3/CH_4 (4 %) was used as the ionization gas for chemical ionization analyses.

Catalytic Substrate Oxidation

In a typical reaction, H_2O_2 in CH_3CN was introduced to a vigorously stirred CH_3CN solution (2.0 mL) containing the iron catalyst, AcOH, and the substrate. The solution was stirred at the temperature of interest until the UV-vis chromophore of **3** completely decayed. The reaction mixture was subsequently treated with 0.1 mL of 1-methylimidazole and 1 mL of acetic anhydride to esterify the alcohol products for GC and GC-MS analyses. Naphthalene was used as an internal standard in these analyses.

RESULTS AND DISCUSSION

Kinetic studies for C–H and C=C oxidation by 3a and 3a*

We have previously reported that the g2.7 species **3a*** (See Figure 1) can be generated from a combination of the iron(II) complex **1a*** and either the H_2O_2/AcOH combination or AcOOH in CH_3CN at −40 °C.[50] The UV-visible, EPR, Mössbauer, and ESI mass spectrometric properties of this species favor its assignment as a low-spin Fe^{III}–OOAc complex. Optical monitoring of the kinetic evolution of **3a*** at its λ_{max} of 460 nm reveals that this species forms rapidly, persists in a steady state, and then undergoes decay once H_2O_2 is depleted (Figure 2). Changes in the concentration of **3a***, as monitored at 460 nm, track well with changes in the integrated EPR signals of samples taken during the course of the reaction,[17] indicating that the optical and EPR spectra arise from the same species. The decay of **3a*** during the last turnover exhibits an exponential behavior, which can be fit to obtain a first-order rate constant of 0.010(1) s^{-1}. Significantly, this observed rate constant does not vary with the nature or concentration of various substrates,[50] indicating that **3a*** does not oxidize substrates directly.

Unlike **3a***, the observed rate constant for the decay of the related **3a** species, which is supported by the less electron-donating TPA ligand, changes upon the introduction of 1-octene (Figure 3a). Upon addition of excess H_2O_2 into a CH_3CN solution of **1a** and AcOH at −40 °C,[50] **3a** is generated, goes into a steady state phase, and then undergoes rapid decay upon depletion of H_2O_2 in the multiple-turnover reaction, analogous to **3a***. Analysis of the kinetic time course for the seemingly exponential decay of **3a** towards the end of the reaction provides a first-order decay rate constant of 0.010 s^{-1} at −40 °C, which increases to 0.032 s^{-1} in the presence of 50 equivalents of 1-octene. At first glance, these results are consistent with the previously reported substrate reactivity of **3a** by Talsi and co-workers,[44] who monitored the intensity of the g_{max} = 2.7 EPR signal of **3a** as a function of time at −70 °C and found the decay rate constant to increase by a factor of 5 in the presence of 12 equivalents of cyclohexene. However, we find that the observed rate constant for **3a**-decay increases further as a function of 1-octene concentration until it reaches a maximum of 0.045 s^{-1}, and then becomes independent of substrate concentration (Figure 3b). This hyperbolic correlation indicates that, analogous to **3a***, **3a** does not oxidize substrates directly and is most likely reversibly connected to the actual oxidizing species.

Interestingly, the lengths of the steady state phase of both **3a** and **3a*** (Figures 2b and 3a) are sensitive to the nature of the substrates. For example, the steady state phase of **3a*** in the presence of the electron-poor *t*-butyl acrylate substrate is almost as long as that in the absence of substrate, but is shortened significantly with the introduction of electron-rich olefins such as cyclooctene and cyclohexene (Figure 2b). Substrate concentration also alters the duration of the steady state phase of **3a***, as can be seen for 1-octene (Figure 2b, black traces). In fact, a linear correlation between the inverse length of the steady state phase and substrate concentration can be obtained for various substrates (Figure 4a). A similar trend is observed in C–H bond oxidation reactions, where substrates with strong C–H bonds such as cyclohexane (BDE ~ 99 kcal/mol)[56] exhibit a longer steady state phase than those with weaker C–H bonds such as cyclohexadiene (BDE = 77 kcal/mol) (Figure 2). Remarkably, an

excellent linear correlation is observed when the ln(1/steady state duration) is plotted *vs.* C–H BDE[56] (Figure 4b, see discussion based on the numerical simulation of the reaction below). Because the inverse of the length of the steady state phase is related to the C–H bond cleavage rate, this plot corresponds to the Bell–Evans–Polanyi plot of log k_{HAT} vs C–H BDE commonly used to describe H-atom transfer reactivity of various oxidants.[57–59] As **3a** and **3a*** do not oxidize substrates directly, the observed changes in the length of their steady state phase as a function of the nature of the substrate and its concentration support the notion that these intermediates are reversibly connected to the species responsible for substrate oxidation.

In order to further explore the role of species **3** in the catalytic olefin oxidation reactions, the formation of the 1,2-epoxyoctane product was monitored as a function of time in the **1a***/H_2O_2/AcOH/1-octene catalytic system via gas chromatography. In agreement with previous results,[50] epoxide formation takes place only when **3a*** is present in the solution (Figure 5a). There is a short lag phase in epoxide formation, during which time **3a*** accumulates to its maximum steady-state level. These results indicate that either **3a*** or a species directly connected to it must be involved in the substrate oxidation step. The duration of the lag phase appears to be dependent on the concentration of the substrate. Numerical simulation analysis (*vide infra*) however shows that the rate of product formation has a minor effect on the length of the lag phase, which suggests that the observed dependence is most likely an experimental artefact that arises due to low detection limits of the gas chromatography. Following the lag phase, the epoxide product forms linearly as a function of time. The rate of epoxide formation correlates linearly with the concentration of 1-octene, indicating a first order dependence on [substrate] (Figure 5b). Replacing CH_3COOH with CH_3COOD does not alter the rate of epoxide formation (Table 2), indicating that the rate determining step of this reaction is not sensitive to the presence of the O–D bond of this additive. An Arrhenius plot of epoxide formation rates gives an activation energy of 54(2) kJ/mol (Figure S2a and Table 2). This value is significantly smaller than the corresponding activation enthalpy for the unimolecular decay of **3a***, which was obtained under identical reaction conditions (Figure S2b and Table 2). Cumulatively, these results indicate that the rate determining step (rds) of the **1a***/H_2O_2/AcOH catalytic system is dominated by the epoxide product formation step at low to moderate equivalents of substrate and involves an oxidizing species that is likely to arise from **3a***.

The reaction mechanism for the **1a***/H_2O_2/AcOH catalytic system appears to be considerably different from that previously deduced for the **1a**/H_2O_2 system.[28] For the latter, activation parameters for the (TPA)Fe^{III}-OOH (**2a**) decay and 1-octene oxide formation were reported to be nearly identical (Table 2). The rate constant of **2a** decay was additionally found to be independent of substrate concentration, and an identical KIE of 2.5 was obtained for both the decay of **2a** and product formation (Table 2). These results are consistent with an rds for the catalytic reaction that involves **2a** decay. Thus, the addition of AcOH into the iron(II)/H_2O_2 reaction mixtures alters the nature of the intermediate that accumulates in a steady-state manner from **2** to **3** by modifying the overall rds of the catalytic reaction. Importantly, an rds that is dominated by the substrate oxidation step at low to moderate

equivalents of substrate, suggests that the oxidizing species may accumulate in the absence of substrate and can therefore be trapped and characterized.

Spectroscopic evidence for the oxidizing species

In an effort to trap and characterize the oxidizing species, reaction mixtures of **1a** or **1a*** with the H_2O_2/AcOH combination were prepared in CH_3CN at −40 °C. Examination of the optical and EPR spectral data for these reaction mixtures revealed no spectroscopic evidence for the presence of a unique intermediate apart from **3a** or **3a***.[50] As the catalytic activities of the (L)Fe^{II}/H_2O_2/AcOH reaction mixtures (L = TPA and BPMEN, See Figure 1) have previously been shown to be essentially identical to that of (L)Fe^{II}/AcOOH,[60] the latter combinations were additionally prepared in an attempt to obtain evidence for the oxidizing species. Unfortunately, UV-vis spectral analysis of these reaction mixtures showed the presence of only the respective Fe^{III}–OOAc species, **3**. However, EPR spectra of **1a***/AcOOH samples frozen at the time point of maximum accumulation of **3a*** based on its 460-nm chromophore showed the presence of two additional sets of EPR signals with *g*-values of 2.07, 2.01 and 1.96 (designated as **5a***, 9% yield relative to **1a***) and 2.21, 2.16 and 1.94 (designated as **6a***, 4% yield relative to **1a***) (Figure 6 and S3). Interestingly, the *g*-values of the corresponding complexes **5a** and **6a** supported by the less electron-donating TPA ligand, which were obtained from the **1a**/AcOOH reaction mixture in CH_3CN at −40 °C, are quite similar to those of **5a*** and **6a*** (Table 3), indicating that the difference in the donicity of the supporting tetradentate ligand (TPA, TPA*) does not affect the EPR parameters of **5** and **6** significantly.

Given that **3a*** is not responsible for substrate oxidation, kinetic studies were subsequently conducted in order to determine which of the two new intermediates, **5a*** or **6a*,** is responsible for substrate oxidation. Aliquots of the **1a***/AcOOH reaction mixture were frozen at various time points and analyzed via EPR spectroscopy. These aliquots revealed a simultaneous accumulation and decay of the EPR signals of **3a***, **5a*** and **6a*** as a function of time, which tracked the growth and decay of the 460-nm chromophore of **3a*** (Figure 6a). These results suggest that the three species most likely exist in a rapid, reversible equilibrium under steady state conditions. When the **1a***/AcOOH reaction mixture was prepared in the presence of various equivalents of 1-octene, the length of the steady state phase of **3a*** (460 nm) decreased with increasing 1-octene concentrations, similar to what was observed for the **1a***/H_2O_2/AcOH reaction mixtures (Figure S4). Importantly, the only EPR signals observed in the presence of 50 equivalents of 1-octene were those of **3a***, while those for **5a*** and **6a*** disappeared (Figure S5), suggesting that either **5a*** or **6a*** could be the oxidizing species in the catalytic reaction. These observations are consistent with EPR studies on the (TPA)*Fe^{III}/H_2O_2/AcOH reaction mixture by Talsi and co-workers,[51] in which a frozen sample of the reaction mixture prepared at −85 °C showed EPR signals belonging to **3a***, **5a*** and **6a***. In agreement with our observations, they found that the introduction of excess 1-octene caused the EPR signals of **5a*** and **6a*** to disappear. Even more importantly, the pseudo-first order rate constants for the decay of the EPR signal of **5a*** showed a linear correlation with 1-octene concentration, providing a second order decay rate constant of 0.032 M^{-1} s^{-1} at −85 °C; unfortunately the kinetic behavior of **6a*** was not reported. While these results are consistent with **5a*** being the species responsible for

oxidizing 1-octene, they do not preclude **6a*** from being the oxidant, as these two species appear to be connected via a rapid equilibrium. We subsequently attempted to probe the electronic structures of these species in order to obtain insight into which of the two intermediates is the key oxidizing species.

In order to achieve a reliable spectroscopic characterization of **5a*** and **6a***, we first attempted to increase the yield of these species beyond the 4 – 10 % obtained in the **1a***/AcOOH combination at −40 °C, and also suppress the accumulation of **3a***. Lowering the reaction temperature to −65 °C in a $CH_3CN/(CH_3)_2CO$ (1:1 v/v) solvent mixture and substituting peracetic acid with cyclohexane peroxycarboxylic acid (CPCA) suppressed the yields of **5a*** and **6a***, but the amount of **3a*** remained relatively unchanged. However, combination of the less electron-rich complex **1a** and CPCA at −65 °C afforded **5a** in a yield of 10 % (relative to **1a**) and suppressed the accumulation of **3a** and **6a** completely (Figure 7 inset). This observation concurs with that of Talsi and co-workers who had previously noted that the relative amounts of **3** and **5** in the (*S,S*-PDP)Fe^{II}/H_2O_2/RC(O)OH catalytic system strongly depended on the steric bulk of the carboxylic acid used. The accumulated results indicate that the proposed equilibrium between **3** and **5** is perturbed by the electronic properties of the supporting ligand as well as the steric bulk of the carboxylate ligand.[52] Importantly, the visible spectrum associated with the reaction solution obtained from the **1a**/CPCA combination shows absorption features at 447, 578 and 730 nm (Figure 7), which decayed completely once the EPR signal of **5a** disappeared. If these UV-vis features belong to **5a** entirely, then respective extinction coefficients of 9000, 5000 and 2000 $M^{-1}cm^{-1}$ can be estimated. These electronic absorption features are in the same spectroscopic region and of similar intensity as those of related g2.07 species **5b** (L = $PyNMe_3$),[54] which exhibits visible bands at 490 nm (ε = 7000 $M^{-1}cm^{-1}$) and 680 nm (ε = 1100 $M^{-1}cm^{-1}$), and $[(TMC)Fe^{V}(O)(NC(O)^tBu)]^+$,[61] which exhibits bands at 425 nm (ε = 4100 $M^{-1}cm^{-1}$), 600 nm (ε = 680 $M^{-1}cm^{-1}$) and 750 nm (ε = 530 $M^{-1}cm^{-1}$). The similarity in the EPR (see Table 3) and electronic absorption parameters of these g2.07 species indicates that **5a** and **5a*** may be electronically related to **5b** and $[(TMC)Fe^{V}(O)(NC(O)^tBu)]^+$, the EPR properties of which strongly argue for an $Fe^{V}(O)$ assignment.[54, 61]

While our approach to obtaining insight into the oxidation state of intermediates **5** and **6** would typically have involved conducting Mössbauer studies, the ~ 4 – 10 % yields of these species make a reliable Mössbauer characterization difficult. Instead, EPR studies were conducted on ^{57}Fe (I = ½)-enriched frozen samples of the **1**/AcOOH reaction mixtures in $CH_3CN/(CH_3)_2CO$ (v/v 1:1). These spectra show that the $g_{mid} = g_y$ = 2.01 features of both **5a** and **5a*** have an identical ^{57}Fe hyperfine splitting corresponding to $|A_y(^{57}Fe)|$ = 65 MHz, while the other two g-values have much smaller A-values. Similarly, the EPR signals of **6a** and **6a*** show an identical hyperfine splitting along the $g_{min} = g_x$ = 1.94 feature corresponding to $|A_x(^{57}Fe)|$ = 60 MHz, with the other two g-values exhibiting smaller A-values. The large A-tensor anisotropy observed, with the largest A-value along the x or y-axis, has previously been used to argue against an $(L^{\bullet+})Fe^{IV}(O)$ electronic structure,[54, 61] which should have comparable A_x and A_y values because of the $d_{xz}^1 d_{yz}^1$ configuration. Indeed, S = ½ $(L^{\bullet+})Fe^{IV}(O)$ species such as the Compounds I of horseradish peroxidase, chloroperoxidase, and cytochrome P450 exhibit *axial* ^{57}Fe A-tensors with $|A_x| \approx |A_y| \gg |A_z|$

(Table 3),[62, 63] which reflect the $d_{xy}^2(d_{xz})^1(d_{yz})^1$ electronic configuration associated with an $S = 1$ $Fe^{IV}(O)$ unit. In contrast, the large *x/y* anisotropy exhibited by **5** and **6** is best rationalized by an $S = ½$ Fe^{III} or Fe^{V} assignment, with the sole unpaired electron occupying either the d_{xz} or d_{yz} orbital.[54] Such an *x/y* anisotropy has been observed for the three other $S = ½$ Fe^{V} complexes $[(TAML)Fe^{V}(O)]^{-}$,[64] $[(TMC)Fe^{V}(O)(NR)]^{+}$,[61] and $(PyNMe_3)Fe^{V}(O)(OAc)$,[54] as well as low-spin Fe^{III} complexes such as $(TPA^*)Fe^{III}$–OOAc (**3a***) and $(N4Py)Fe^{III}$–OOH (Table 3).[50, 65] The EPR *g*-values of **6** fit well to the Griffith-Taylor model for low-spin iron(III) complexes,[50, 54] which considers spin-orbit coupling within a T_{2g} set that is energetically well separated from the E_g set and low-lying charge transfer states.[66, 67] In contrast, the *g*-values of complexes **5a** and **5a*** do not fit well to the Griffith-Taylor model, but are similar to those of the two characterized $Fe^{V}(O)$ complexes $[(TAML)Fe^{V}(O)]^{-}$ [64] and $[(TMC)Fe^{V}(O)(NR)]^{+}$,[61] as well as $(PyNMe_3)Fe^{V}(O)(OAc)$, **5b**, described by Serrano *et al.*,[54] which argue for their assignment as oxoiron(V) species.

Our proposed assignment of **5a** and **5a*** as $Fe^{V}(O)$ complexes is consistent with their observed reactivity towards hydrocarbon substrates. In particular, **5a*** has previously been reported by Talsi to react with 1-octene with a relatively large rate constant of 0.032 $M^{-1}s^{-1}$ at −85 °C.[51] We also find cyclooctene oxidation by the **1a***/AcOOH mixture to afford a large yield of cyclooctene oxide, along with a minor amount of *cis*-2-acetoxycyclooctanol. The latter incorporates a CD_3CO_2 group (31 %), when a $CH_3C(O)OOH/CD_3COOH$ mixture is used. Formation of the *cis*-2-acetoxycyclooctanol product most likely involves transfer of *cis*-disposed oxo and acetato ligands of **5a*** to the olefinic C=C bonds via a [3+2] cycloaddition pathway.[68, 69] The incorporation of deuterated acetate into the *cis*-2-acetoxycyclooctanol product presumably involves an acetate ligand exchange that takes place at the $Fe^{V}(O)(OAc)$ stage, as peracetic acid does not readily exchange with CD_3CO_2D even in the presence of a Lewis acid,[54] so acetate exchange between Fe^{III}–OOAc and CD_3CO_2D is highly unlikely. These results also support the $Fe^{V}(O)(OAc)$ formulation for **5a** and **5a***.

The reactivity patterns of **5a** and **5a*** dovetail well with those of $(PyNMe_3)Fe^{V}(O)$ complex **5b**, which is generated from the reaction of the $Fe^{II}(PyNMe_3)$ precursor **1b** with peracids.[54] Apart from exhibiting EPR spectroscopic parameters and ^{57}Fe hyperfine splittings that are nearly identical to those of **5a** and **5a*** (Table 3), **5b** has also been shown to oxidize cyclohexane with a bimolecular rate constant of 2.8 $M^{-1}s^{-1}$ at −40 °C, which is the largest rate constant for cyclohexane oxidation observed to date for high-valent iron species. **5b** also oxidizes cyclooctene with a large bimolecular rate constant of 375 $M^{-1}s^{-1}$ at −60 °C to afford cyclooctene oxide,[73] along with minor amounts of *cis*-2-acetoxycyclooctanol that become partially deuterated (10 %) when an $AcOOH/CD_3COOD$ mixture is used. Given the $Fe^{V}(O)(OAc)$ electronic structure deduced for **5b**,[54] the similar spectroscopic parameters and reactivity patterns of **5a**, **5a*** and **5b** argue for the analogous $Fe^{V}(O)(OAc)$ electronic structure assignment for these intermediates. We thus propose **5** to be the active oxidant in the catalytic hydrocarbon oxidation reactions we have described.

Kinetic studies on the role of the Fe^{III}–OOAc complex, 3

Further kinetic studies have been conducted in order to obtain insight into the role of **3** in the **1**/H_2O_2/AcOH catalytic reaction, as well as its relation to the oxidizing species, **5**. We began by investigating the formation mechanism of **3a*** from **1a***, H_2O_2 and AcOH. Careful analysis of the optical spectra obtained during the formation of **3a*** in the **1a***/H_2O_2/AcOH reaction mixture at −40 °C did not reveal the presence of a unique UV-vis feature that would correspond to an intervening species.[50] EPR analysis of aliquots of this reaction mixture frozen at appropriately chosen time-points, however, showed the presence of additional EPR signals at g = 2.18, 2.15, 1.97, which correspond to the (TPA*)Fe^{III}–OOH species, **2a*** (Figure S6).[50] The involvement of the Fe^{III}–OOH intermediate during the formation of Fe^{III}–OOAc complexes was even more obvious in reactions involving complex **1a** supported by the less electron-rich TPA ligand. The UV-vis spectrum of the **1a**/H_2O_2/AcOH reaction mixture at −40 °C revealed the presence of a broad optical feature at λ_{max} ~ 540 nm, which is characteristic of the (TPA)Fe^{III}–OOH species **2a** (Figure 8).[24] An EPR analysis of aliquots of this reaction mixture also showed the unique EPR signals of **2a** at $g_{\perp}$ = 2.15 and $g_{\parallel}$ = 1.97, which accumulated and decayed along the same time frame as those of **3a** (Figure 8, inset).[34] These results suggest that low-spin Fe^{III}–OOH complexes are likely precursors to the S = ½ Fe^{III}–OOAc complexes **3a** and **3a***.

If low-spin Fe^{III}–OOH species **2** were competent intermediates during the formation of the Fe^{III}–OOAc complexes **3**, then the addition of AcOH to independently generated Fe^{III}–OOH species should also furnish the acylperoxoiron(III) complexes. Consistent with this hypothesis, the addition of excess AcOH into CH_3CN solutions of **2a** and **2a*** at −40 °C led to a rapid accumulation of the ~460-nm chromophore of the respective Fe^{III}–OOAc complexes (Figure 9 and S7). However, the time frames for the decay of **2a** and for the formation of **3a** were substantially different, indicating that **2a** does not directly convert to **3a**. The presence of an intermediate in this transformation is made apparent by a careful inspection of the UV-vis spectrum, which shows a rapid increase in absorbance at 370 nm concomitant with the decay of absorbance at 540 nm arising from **2a**. This intermediate, designated as **4a**, subsequently decays on a longer time frame to afford **3a**. In the analogous reaction of **2a*** with excess AcOH (Figure S7), the extensive overlap between the broad chromophores of **2a*** and **3a*** masks the observation of an intermediate during this transformation. EPR analysis of aliquots of the **2a**/AcOH reaction mixture, collected at −40 °C and frozen at appropriately chosen time-points showed decay of the S = ½ EPR signals of **2a** (g_{max} ~ 2.15), along with the appearance of the EPR signals of **3a** (g_{max} = 2.74); the latter subsequently disappeared within a time-scale of ~ 400 seconds in agreement with the UV-vis kinetic time course (Figure S8). However, no other S = ½ EPR signals were detected during the decay of **2a** and the formation of **3a**. Cumulatively, these results show that **3a** is formed from the combination of **2a** and AcOH via **4a**. Current reaction conditions, however, do not lead to the generation of **4a** in sufficient yield and purity to ascertain its electronic structure.

As a detailed spectroscopic characterization of **4** is currently not possible, we have employed an alternative approach to obtain insight into the electronic structure of this species by performing an extensive kinetic study of the AcOH-assisted decay of **2a** to form **4a**. Given

that the rapid decay of **2a** is kinetically isolated from the relatively slow formation of **3a**, the pseudo unimolecular decay rate constant of **2a** can be reliably obtained via exponential fitting of the 540-nm time trace. A good single exponential fit for the decay of **2a** in the presence of 200 equiv. of AcOH can indeed be obtained (Figure 9, inset, yellow trace), which provides a pseudo first-order decay rate constant of 0.17(1) s^{-1}. This matches the rate constant for the formation of intermediate **4a** as obtained from an exponential fitting of the rapid increase in absorbance at 370 nm. The decay rate constant of **2a** varies with AcOH concentration and shows a saturation type behavior (Figure 10) that provides a maximum decay rate constant of 0.28 s^{-1}. This represents a ~900-fold enhancement in the decay of **2a** due to the presence of AcOH. The role of AcOH as a proton donor in **2a**-decay is further demonstrated by an H/D kinetic isotope effect of 1.7(1) upon substitution of AcOD for AcOH (100 or 200 equiv.). When monitored as a function of temperature, the decay of **2a** in the presence of 200 equiv. AcOH takes place with a relatively small activation enthalpy of 25(2) kJ/mol and a large, negative activation entropy of −151(10) J/mol•K (Figure S9), which is consistent with an associative process. Thus, the formation of intermediate **4a** involves a fast reversible association of AcOH and **2a**, followed by a slower, proton-assisted decay step.

The formation mechanism we deduce for intermediate **3a** parallels that proposed by Wang and Shaik for the generation of the low-spin (*S,S*-PDP)Fe^{III}–OOAc species based on DFT calculations.[74] They found that the most energetically favorable pathway for the AcOH-assisted decay of the (*S,S*-PDP)Fe^{III}–OOH precursor involved homolytic cleavage of the O–O bond to yield H_2O and an $S = 1/2$ Fe^{IV}(O)(•OAc) species with a calculated KIE of 3.3. Subsequent O–O bond coupling occurs with a relatively small energy barrier to generate the Fe^{III}–OOAc species (Scheme 1). Accordingly, we tentatively formulate **4** as an Fe^{IV}(O)(•OAc) species but can only associate it with a fleeting absorbance at 370 nm. Additional studies aimed at confirming the assignment of this intermediate and gaining further insight into its electronic structure are ongoing.

Numerical simulation of the kinetic traces of 3a* in the presence of 1-octene

In order to obtain further clarity on the roles of the Fe^{III}–OOAc and Fe^{V}(O)(OAc) species in the Fe^{II}/H_2O_2/AcOH catalytic system, we have devised a chemical scheme (Scheme 2) based upon the aforementioned kinetic studies describing the formation of the g2.7 species (**3a**/**3a***), its lack of reactivity with C–H and C=C bonds,[50] and its necessary evolution to the g2.07 species (**5a**/**5a***) that actually carries out substrate oxidation. Using this chemical model, we can rationalize the curious kinetic behavior of **3a***, where the duration of its steady state phase decreases as a function of the nature of the substrate and its concentration without an apparent enhancement in the observed rate constant of its ultimate decay (Figure 2). The comparatively high yield of **3a*** and the well-defined steady state segment makes this reaction the best choice for simulation of the time course.

A numerical integration simulation approach has been utilized where the rate constants for the steps in Scheme 2 are varied to produce the best least-squares fit to the experimental data. The initial parameters for some of the kinetic steps were obtained from previous experimental values[34] and from experiments describing the formation of (TPA)Fe^{III}–OOAc

from (TPA)Fe^{III}–OOH and AcOH in this study. This model successfully simulates the variation in the kinetic time traces of **3a*** as a function of [1-octene] (Figure 11). The details of the fitting method are described in the SI. The fitted rate constants for the individual steps in this kinetic model are presented in Table 4. A few of the rate constants, especially those in the beginning of the catalytic cycle (k_1, k_2, k_3) can be varied significantly without altering the fit to the data. With the use of the same model and rate constants, a comparably good fit of the data can also be obtained for the oxidation of 1-octene shown in Figure 2b at double the catalyst concentration (Figure S10). The good fit between the numerical simulations and the experimental data presented in Figures 2 and 11 show that the mechanism presented in Scheme 2 is plausible and consistent with the experimental data. Alternative chemical models shown in Schemes S2 and S3 were also considered as possible solutions, but they did not prove successful. The presence of an equilibrium between the tautomeric species **4a*** and **5a*** means that **4a*** in Scheme 2 cannot be ruled out as a reactive species. As **4a*** is only present in a very small concentration, it is difficult to clarify its nature. However there is growing evidence that nonheme oxoiron(V) species are observable (see Table 3), and several are powerful enough to carry out the oxidation reactions studied here.[54,64,70] The latter point leads us to favor **5a*** as the likely key oxidant of the catalytic reaction, so the following discussion focuses on **5a***.

The first step in the catalytic cycle depicted in Scheme 2 (k_1) involves oxidation of the iron(II) precursor **1a*** by H_2O_2 to afford the one-electron-oxidized (L)Fe^{III}–OH species. The facile conversion of Fe^{II} catalysts supported by tetradentate N4 ligands to their catalytically active Fe^{III} forms in the presence of peroxo-based oxidants such as H_2O_2, AcOOH and *m*CPBA has been demonstrated numerous times.[22, 23, 25, 51, 54] The fitted rate constant for this step is indeed in the range reported for the conversion of **1b** into ($PyNMe_3$)Fe^{III}–OH, as well as the conversion of iron(II) complexes supported by tetradentate N4 ligands BPMEN and PDP to the corresponding Fe^{III}–OOH species, assuming that the following step is relatively fast (see Table 4). The subsequent generation of the Fe^{III}–OOH complex **2a*** (k_2 and k_{-2}) requires an additional equivalent of H_2O_2.[22, 23, 25, 54, 75, 76] This step essentially entails substitution of an –OH for an–OOH ligand via an acid-base type of transformation and is significantly faster than the previous step.

The next step involves the binding of AcOH to the available solvent site on **2a*** to form an AcOH adduct of **2a***(AcOH) (k_3 and k_{-3}), which then decays to intermediate **4a*** (k_4 and k_{-4}). The experimentally determined unimolecular **2a** decay rate constant of 0.28 s^{-1} under saturating AcOH concentrations (Figure 10) is not too different from the value of 0.137 s^{-1} obtained for the decay of an AcOH adduct of **2a*** to form **4a*** via numerical simulation (Table 4). This is the step that exhibits an AcOH/AcOD KIE of 1.7 in Table 2. On the basis of kinetic and spectroscopic studies, intermediate **4a** is shown to possess an optical chromophore at 370 nm. This species has been formulated to be Fe^{IV}(O)(•OAc) based on the nature of its decay products (discussed in the next paragraph) and the DFT calculations by Wang and Shaik.[74]

Intermediate **4a*** can be converted into three distinct species. The first (k_6) involves irreversible decarboxylation of the carboxyl radical to afford CO_2, an alkyl radical and Fe^{IV}(O). This pathway is required to account for the finite steady state lifetime of species

3a* at the end of the multiple turnover cycle in the absence of substrate. The existence of this pathway is supported by the formation of $[(TPA)Fe^{IV}(O)(NCMe)]^{2+}$ and benzaldehyde in respective 70% and 90% yields relative to **1a** when acetic acid is replaced by phenylacetic acid,[77] where the benzaldehyde product arises from trapping of the relatively stable benzyl radical with dioxygen.[34, 78, 79] On the other hand, when acetic acid is substituted by perfluorobenzoic acid, formation of C_6F_5OH is observed, which derives from the more reactive aryl radical undergoing rebound onto the nascent $Fe^{IV}(O)$ species, resulting in catalytic C_6F_5OH formation.[34, 78, 79] The introduction of olefins into either reaction mixture was shown to decrease the yields of both radical-derived products,[34, 79] indicating that oxidative decarboxylation and olefin epoxidation are competitive processes. Importantly, these results support the involvement of an $Fe^{IV}(O)(^{\bullet}OAc)$ species (tentatively assigned as **4** in Scheme 2) in the catalytic cycle that is reversibly connected to the species responsible for olefin oxidation.

The second decay pathway for the $Fe^{IV}(O)(^{\bullet}OAc)$ species (k_7 and k_{-7}) involves valence tautomerization to the $Fe^{V}(O)(OAc)$ electromer **5a***,[50] the forward rate constant k_7 being five-fold larger than k_6 in the numerical simulation (Table 4). Satisfactory fits were obtained only if this step is reversible. Complex **5a** exhibits an EPR signal with *g*-values of 2.07, 2.01 and 1.96, which can be associated with a visible chromophore with features at 447, 578 and 730 nm, (Figure 7). The EPR *g*-values and ^{57}Fe-hyperfine splitting for **5a** and **5a*** are identical to each other.[51, 52, 54, 73] Importantly, **5a*** was shown by Talsi and co-workers to oxidize 1-octene with a rate constant of 0.032 $M^{-1}s^{-1}$ at −85 °C,[51] which is consistent with the 20-fold larger fitted second order rate constant of 0.77 $M^{-1}s^{-1}$ we obtained at −40 °C (Table 4). The congruence of these two rate constants supports the notion that **5a*** is the key oxidant in the **1a***/H_2O_2/AcOH reaction mixture.

The third decay pathway (k_5 and k_{-5}) involves an O–O bond formation to re-generate the Fe^{III}–OOAc species **3a***, which occurs at a comparable rate as the step associated with k_6 (Table 4).[74] The fitting analysis of the kinetic data requires reversible interconversion between the $Fe^{IV}(O)(^{\bullet}OAc)$ complex and the Fe^{III}–OOAc species, in agreement with previous DFT calculations.[50, 74] Indeed, the reverse rate constant (k_{-5}) of 0.016 s^{-1} found by numerical simulation approaches the observed rate constant of 0.010(1) s^{-1} obtained by exponential fitting of the A460 time-trace associated with **3a*** decay upon depletion of H_2O_2 at the end of the multiple turnover reaction. The model suggests that the decay time course of species **3a*** when H_2O_2 is depleted will be affected not only by k_{-5}, but also by k_5, k_6, k_7, k_{-7} and k_8. This is true because all of these rate constants, as well as the substrate concentration, affect the rate of reformation of **3a*** as it is decaying. The time course appears to be exponential because all of the rate constants involved are first order or pseudo-first order under the conditions of the experiment. As it turns out, the relative magnitudes of these rate constants cause the decay of **3a*** to follow approximately the same time course over a wide range of substrate concentrations, making the experimental rate constants appear to be invariant (Figure 2). The exponential fit of the composite decay time course gives a slightly less than the true value for k_{-5}. For species **3a**, this observed decay rate constant, which is also a composite of the rate constants k_{-5}, k_5, k_6, k_7, k_{-7} and k_8 initially responds

to changes in substrate concentration but then becomes invariant at higher concentrations (Figure 3).

The decay of the Fe^{III}–OOAc complex therefore involves a dynamic equilibrium among the Fe^{III}–OOAc (**3**), $Fe^{IV}(O)(^{\bullet}OAc)$ (**4**) and $Fe^{V}(O)(OAc)$ (**5**) components of the catalytic troika, as depicted in Scheme 2. The existence of this equilibrium is additionally supported by monitoring the steady state yield of the Fe^{III}–OOAc intermediate **3a*** as a function of substrate concentration. In particular, the maximum yield of the Fe^{III}–OOAc species is dictated by the relative rate constants for the formation and decay of Fe^{III}–OOAc (k_5 and k_{-5}) and $Fe^{V}(O)(OAc)$ (k_7 and k_{-7}) from the $Fe^{IV}(O)(^{\bullet}OAc)$ species, as well as the rate constant of substrate oxidation by $Fe^{V}(O)(OAc)$ (k_8). According to this model, the accumulation of **3a*** should be sensitive to the rate of substrate oxidation by **5a***. Thus, varying the concentration of substrate and its C–H bond strength should alter this rate. Indeed, at high concentrations of an easily oxidizable substrate like 1,4-cyclohexadiene with a C–H bond dissociation energy of 77 kcal/mol, the maximum yield of **3a*** under steady state conditions was observed to decrease by ~ 50 % (Figure 12). Numerical simulation of the time course of **3a*** as a function of [cyclohexadiene] using the model shown in Scheme 2 affords a C–H bond cleavage rate of 88 $M^{-1}s^{-1}$ (Figure S11), which is two orders of magnitude larger than the second order rate constant for 1-octene oxidation (0.7 $M^{-1}s^{-1}$). A decrease in the maximum yield of **3a*** thus occurs because the decay rate constant of the $Fe^{V}(O)(OAc)$ species becomes much larger in magnitude than its reverse rate constant of conversion to the $Fe^{IV}(O)(^{\bullet}OAc)$ species at higher concentrations of the substrate, in effect shifting the equilibrium away from Fe^{III}–OOAc in Scheme 2. Similarly, in the **1a**/H_2O_2/AcOH/1-octene catalytic system, the maximum yield of **3a** under steady state conditions decreases as the concentration of 1-octene is increased (Figure S12). Thus, the formation of the Fe^{III}–OOAc species **3** and substrate oxidation by the $Fe^{V}(O)(OAc)$ electromer must be competitive, which in turn indicates that these species are reversibly connected.

The dynamic equilibrium among the Fe^{III}–OOAc, $Fe^{V}(O)(OAc)$, and $Fe^{IV}(O)(^{\bullet}OAc)$ species is responsible for the curious kinetic evolution of the Fe^{III}–OOAc complex (Figures 2, 3, 4 and 11), where the length of the steady state phase responds to the nature and concentration of the substrate. In particular, as substrate oxidation by the $Fe^{V}(O)(OAc)$ species is the predominant contributor to the rate-determining step of the entire reaction under the conditions studied here (see Figure 5b), the rate of this step controls the consumption rate of the H_2O_2 reagent, thereby dictating the duration of each turnover cycle. With a fixed amount of H_2O_2, a faster single turnover cycle reduces the duration of the overall multiple turnover reaction, in effect decreasing the duration of the steady-state accumulation of Fe^{III}–OOAc that is in equilibrium with the $Fe^{V}(O)(OAc)$ oxidant. As a consequence, the inverse length of the steady state phase of **3** is proportional to the rate constant for substrate oxidation. The inverse of the duration of the steady state phase thus becomes a surrogate for $k_{(}$substrate oxidation), and a linear plot of ln(surrogate k) vs BDE can be observed (Figure 4b) that essentially corresponds to the Bell–Evans–Polanyi plots commonly used to describe the C–H bond cleavage reactivity of a variety of high-valent iron oxidants.[57–59, 80] Species **3** effectively reaches an equilibrium with **4**, which slows the reaction by decreasing the

concentration of the key oxidant **5** in solution, but has little effect on the reaction flux after this equilibrium is established.

The formation of the diiron(III) species **7** is included in the chemical model as it helps to account for the slight loss in the steady state accumulation of **3** during the course of the multiple turnover reaction. It also explains the residual absorbance at 460 nm at the end of the reaction. Indeed ESI-MS analysis of the reaction mixture at the end of the reaction shows the major decay product to be $[(TPA^*)_2Fe^{III}_2(\mu\text{-}O)(\mu\text{-}OAc)]^{3+}$ (Figure S13), which possesses an absorption maximum at ~460 nm[81, 82] and has been shown to be catalytically inactive towards the substrates tested in this study.[34, 83]

The numerical simulation results on 1-octene oxidation can also be used to obtain insights into the oxidation rates of other substrates. For example, the longer steady state phase observed for the oxidation of 250 mM cyclohexane in Figure 2b can be reproduced assuming a 1-octene concentration of 25 mM (Figure S10), suggesting that the oxidation rate for cyclohexane is about an order of magnitude slower than that of 1-octene. Indeed comparable rate differences for the oxidation of 1-octene versus cyclohexane have been found for two other high-valent iron-oxo oxidants. The high-spin $[Fe^{IV}(O)(TQA]$ complex oxidizes 1-octene 16-fold faster than cyclohexane at −40 °C,[59] while the $Fe^{V}(O)$ oxidant generated from $Fe(PyNMe_3)$ and AcOOH is about 40-fold faster in the oxidation of 1-octene than cyclohexane.[54.73] Furthermore, a competitive oxidation experiment suggested by a reviewer of equimolar amounts of *tert*-butyl acrylate and cyclohexane shows a 2:1 ratio of acrylate oxidation products over cyclohexane oxidation products, confirming that the rate constants for oxidation of *tert*-butyl acrylate and cyclohexane are comparable within the error of these measurements, consistent with the data in Figure 2b.

We have attempted to include the minor species **6** in the kinetic modelling of Scheme 2. The numerical simulations indicate that placing **6a*** at any of several positions in the pathway in equilibrium with species **3a***, **4a*** or **5a*** had minimal effect on the quality of the simulation shown in Figure 11. Rate constants of other steps in the reaction (Table 4) were nearly unaltered. Given the low yield of **6a*** (4%), the lack of information regarding its electronic structure, its lack of reactivity with substrates, as well as uncertainty of its position in the reaction pathway, we believe that addition of **6a*** to Scheme 2 would be too speculative. None of the major findings of this study are impacted by omission of species **6a*** from Scheme 2.

SUMMARY AND PERSPECTIVES

Our cumulative kinetic and spectroscopic studies have facilitated a determination of the roles that the g2.7 and the g2.07 species play in the Fe^{II}/H_2O_2/AcOH catalytic system. These results show that the g2.7 species **3a** and **3a*** do not oxidize substrates directly, but are instead off-pathway in the catalytic transformations. The relevance of the g2.7 species in catalytic reactions should therefore not be over-emphasized. The g2.07 subset on the other hand has been demonstrated to be the key oxidizing species in the catalytic reaction. This species exhibits EPR *g*-values at ca. 2.07, 2.01 and 1.96, which are insensitive to the electronic properties of the supporting ligands, as well as visible spectral features at 447,

578 and 730 nm. These spectral features resemble those of better characterized $Fe^{V}(O)$ complexes **5b** (L = $PyNMe_3$) and $[(TMC)Fe^{V}(O)(NC(O)^{t}Bu)]^{+}$. The similarity of the spectroscopic properties of **5a** and **5a*** with those of **5b** and $[(TMC)Fe^{V}(O)(NC(O)^{t}Bu)]^{+}$ favor the assignment of **5a** and **5a*** as $Fe^{V}(O)(OAc)$ species. Importantly, these g2.07 species **5** have been demonstrated to be in a reversible equilibrium with the Fe^{III}–OOAc complexes, **3**. The equilibrium is shown to be perturbed by the electronic properties of the supporting tetradentate ligand and the steric properties of carboxylic acids.[52] The previously reported reactivity differences between the Fe^{III}–OOAc complexes **3a** and **3a*** can thus be attributed to the existence of the equilibrium between **3** and **5**.[44, 50] In particular, the linear dependence of the rate constant for **3a** decay as a function of substrate concentration (low concentration range) does not arise from a direct reaction with substrate, but instead arises from the enhancement in the rate of **5** decay. The apparent rate constant for **3** decay is a composite of multiple rate constants as a result of the equilibrium between species **3**, **4** and **5**.

The current study shows that the g2.7 and g2.07 EPR species resulting from the reaction of H_2O_2 and AcOH with **1a** and **1a*** differ in both structure and reactivity. Observation of ^{57}Fe- hyperfine splitting on *only one* of the three g-values for these species formed by using ^{57}Fe-enriched catalysts indicates that neither is the $Fe^{IV}(O)(\bullet OAc)$ species favored by others.[51, 52] This hyperfine splitting pattern is instead consistent with either a low-spin Fe^{III} or Fe^{V} assignment. Accordingly, spectroscopic analysis and comparisons with characterized model complexes[54, 61] suggest that the g2.7 species correlated with intermediates **3a** and **3a*** is a low-spin Fe^{III}–OOAc species, while the g2.07 intermediate correlated with intermediates **5a** and **5a*** is a $Fe^{V}(O)(OAc)$ species. Our kinetic analysis of the evolution of the **3a*** intermediate (Figures 2b, 6 and 11) reveals that **3** and **5** must exist in a dynamic equilibrium that is modulated by the nature of the supporting ligand. Moreover, it is shown that the true reactive species of this system, and probably of all similar carboxylic-acid-modulated mononuclear iron catalyst systems, is the high-valent $Fe^{V}(O)$ intermediate, **5**.

Similar to the synthetic transformations discussed here, the role of peroxoiron(III) and oxoiron(V) intermediates in C–H and C=C oxidations mediated by the biological Rieske oxygenases are not yet clear.[5] As mentioned previously, side-on bound O_2 adducts of enzyme-substrate complexes of naphthalene 1,2-dioxygenase and carbazole 1,9a-dioxygenases have been trapped in crystals.[8, 9] These adducts are speculated to correspond to the (hydro)peroxoiron(III) intermediate observed in the “peroxide shunt” reaction of fully oxidized benzoate 1,2-dioxygenase, which is capable of producing one turnover of the expected *cis*-diol product.[10] It is unclear whether the peroxoiron(III) intermediate is responsible for oxidizing the substrates or if this species undergoes O–O bond breaking to afford an $Fe^{V}(O)(OH)$ oxidant. Experimental evidence, however exists that support the model of an $Fe^{V}(O)$ oxidant in these enzymes based upon the observed incorporation of ^{18}O from $H_2{}^{18}O$ into the oxidation products of indan (68 % into 1-indanol product of monooxygenase chemistry) by toluene dioxygenase[29] and naphthalene (3 % into *cis*-1,2-dihydrodiol product of dioxygenase chemistry) by naphthalene dioxygenase during a peroxide shunt reaction.[30] These results show that an $Fe^{V}(O)$ species similar to **5** in our study could plausibly act as the key oxidant in the chemistry of Rieske oxygenases. The

findings presented here, therefore, have significance for the design of catalysis to carry out regio- and stereo-specific reactions, as well as for the goal of understanding the mechanisms of the remarkably versatile oxidants formed by nature's most potent oxygenases.

Supplementary Material

Refer to Web version on PubMed Central for supplementary material.

Acknowledgments

Financial support for this work was provided by grants from the Department of Energy, Office of Basic Energy Sciences (DE-FG02-03ER15455 to L.Q.), the National Science Foundation (CHE-1361773 and CHE-1665391 to L.Q.), and National Institutes of Health (GM40466 and GM100943 to J.D.L.)

References

1. Sono M, Roach MP, Coulter ED, Dawson JH. Chem Rev. 1996; 96:2841–2887. [PubMed: 11848843]
2. Solomon EI, Brunold TC, Davis MI, Kemsley JN, Lee SK, Lehnert N, Neese F, Skulan AJ, Yang YS, Zhou J. Chem Rev. 2000; 100:235–349. [PubMed: 11749238]
3. Costas M, Mehn MP, Jensen MP, Que L Jr. Chem Rev. 2004; 104:939–986. [PubMed: 14871146]
4. Kovaleva EG, Lipscomb JD. Nature Chem Biol. 2008; 4:186–193. [PubMed: 18277980]
5. Barry SM, Challis GL. ACS Catal. 2013; 3:2362–2370.
6. Kal S, Que L. J Biol Inorg Chem. 2017; 22:339–365. [PubMed: 28074299]
7. Ferraro DJ, Gakhar L, Ramaswamy S. Biochem Biophys Res Commun. 2005; 338:175–190. [PubMed: 16168954]
8. Karlsson A, Parales JV, Parales RE, Gibson DT, Eklund H, Ramaswamy S. Science. 2003; 299:1039–1042. [PubMed: 12586937]
9. Ashikawa Y, Fujimoto Z, Usami Y, Inoue K, Noguchi H, Yamane H, Nojiri H. BMC Struct Bio. 2012; 12:15. [PubMed: 22727022]
10. Neibergall MB, Stubna A, Mekmouche Y, Münck E, Lipscomb JD. Biochemistry. 2007; 46:8004–8016. [PubMed: 17567152]
11. Rivard BS, Rogers MS, Marell DJ, Neibergall MB, Chakrabarty S, Cramer CJ, Lipscomb JD. Biochemistry. 2015; 54:4652–4664. [PubMed: 26154836]
12. Que L Jr, Tolman WB. Nature. 2008; 455:333–340. [PubMed: 18800132]
13. Sun CL, Li BJ, Shi ZJ. Chem Rev. 2011; 111:1293–1314. [PubMed: 21049955]
14. Talsi EP, Bryliakov KP. Coord Chem Rev. 2012; 256:1418–1434.
15. Oloo, WN., Que, L, Jr. Hydrocarbon Oxidations Catalyzed by Bio-Inspired Nonheme Iron and Copper Catalysts. In: Reedijk, J., Poeppelmeier, K., editors. Comprehensive Inorganic Chemistry II. Vol. 6. Elsevier; Oxford: 2013. p. 763-778.
16. Gelalcha FG. Adv Synth Catal. 2014; 356:261–299.
17. Oloo WN, Que L Jr. Acc Chem Res. 2015; 48:2612–2621. [PubMed: 26280131]
18. Cusso O, Ribas X, Costas M. Chem Commun. 2015; 51:14285–98.
19. Wolfe MD, Lipscomb JD. J Biol Chem. 2003; 278:829–835. [PubMed: 12403773]
20. Sobolev AP, Babushkin DE, Talsi EP. Mendeleev Commun. 1996:33–34.
21. Kim C, Chen K, Kim J, Que L Jr. J Am Chem Soc. 1997; 119:5964–5965.
22. Chen K, Que L Jr. J Am Chem Soc. 2001; 123:6327–6337. [PubMed: 11427057]
23. Chen K, Costas M, Kim J, Tipton AK, Que L Jr. J Am Chem Soc. 2002; 124:3026–3035. [PubMed: 11902894]
24. Mairata i Payeras A, Ho RYN, Fujita M, Que L Jr. Chem Eur J. 2004; 10:4944–4953. [PubMed: 15372680]

25. Makhlynets OV, Rybak-Akimova EV. Chem Eur J. 2010; 16:13995–14006. [PubMed: 21117047]
26. Hitomi Y, Arakawa K, Funabiki T, Kodera M. Angew Chem Int Ed. 2012; 51:3448–3452.
27. Zang C, Liu Y, Xu ZJ, Tse CW, Guan X, Wei J, Huang JS, Che CM. Angew Chem Int Ed. 2016; 55:10253–10257.
28. Oloo WN, Fielding AJ, Que L Jr. J Am Chem Soc. 2013; 135:6438–6441. [PubMed: 23594282]
29. Wackett LP, Kwart LD, Gibson DT. Biochemistry. 1988; 27:1360–1367. [PubMed: 3365392]
30. Wolfe MD, Lipscomb JD. J Biol Chem. 2003; 278:829–835. [PubMed: 12403773]
31. Company A, Gomez L, Güell M, Ribas X, Luis JM, Que L Jr, Costas M. J Am Chem Soc. 2007; 129:15766–15767. [PubMed: 18052284]
32. Prat I, Mathieson JS, Güell M, Ribas X, Luis JM, Cronin L, Costas M. Nature Chem. 2011; 3:788–793. [PubMed: 21941251]
33. White MC, Doyle AG, Jacobsen EN. J Am Chem Soc. 2001; 123:7194–7195. [PubMed: 11459514]
34. Mas-Ballesté R, Que L Jr. J Am Chem Soc. 2007; 129:15964–15972. [PubMed: 18052063]
35. Chen MS, White MC. Science. 2007; 318:783–787. [PubMed: 17975062]
36. Gomez L, Garcia-Bosch I, Company A, Benet-Buchholz J, Polo A, Sala X, Ribas X, Costas M. Angew Chem Int Ed. 2009; 48:5720–5723.
37. Chen MS, White MC. Science. 2010; 327:566–571. [PubMed: 20110502]
38. White MC. Science. 2012; 335:807–809. [PubMed: 22344434]
39. Wu M, Miao CX, Wang S, Hu X, Xia C, Kühn FE, Sun W. Adv Synth Catal. 2011; 353:3014–3022.
40. Lyakin OY, Ottenbacher RV, Bryliakov KP, Talsi EP. ACS Catal. 2012; 2:1196–1202.
41. Cussó O, Garcia-Bosch I, Ribas X, Lloret-Fillol J, Costas M. J Am Chem Soc. 2013; 135:14871–14878. [PubMed: 24060452]
42. Wang B, Wang S, Xia C, Sun W. Chem Eur J. 2012; 18:7332–7335. [PubMed: 22581474]
43. Cussó O, Ribas X, Lloret-Fillol J, Costas M. Angew Chem Int Ed. 2015; 54:2729–2733.
44. Lyakin OY, Bryliakov KP, Britovsek GJP, Talsi EP. J Am Chem Soc. 2009; 131:10798–10799. [PubMed: 19722657]
45. Lyakin OY, Bryliakov KP, Talsi EP. Inorg Chem. 2011; 50:5526–5538. [PubMed: 21598909]
46. Guisado-Barrios G, Zhang Y, Harkins AM, Richens DT. Inorg Chem Commun. 2012; 20:81–85.
47. Lyakin OY, Prat I, Bryliakov KP, Costas M, Talsi EP. Cat Commun. 2012; 29:105–108.
48. Makhlynets OV, Oloo WN, Moroz YS, Belaya IG, Palluccio TD, Filatov AS, Müller P, Cranswick MA, Que L Jr, Rybak-Akimova EV. Chem Commun. 2014; 50:645–648.
49. Bryliakov KP, Talsi EP. Coord Chem Rev. 2014; 276:73–96.
50. Oloo WN, Meier KK, Wang Y, Shaik S, Münck E, Que L Jr. Nat Commun. 2014; 5:4041–4049. [PubMed: 24909383]
51. Lyakin OY, Zima AM, Samsonenko DG, Bryliakov KP, Talsi EP. ACS Catal. 2015; 5:2702–2707.
52. Zima AM, Lyakin OY, Ottenbacher RV, Bryliakov KP, Talsi EP. ACS Catal. 2016; 6:5399–5404.
53. Zima AM, Lyakin OY, Ottenbacher RV, Bryliakov KP, Talsi EP. ACS Catal. 2017; 7:60–69.
54. Serrano-Plana J, Oloo WN, Acosta-Rueda L, Meier KK, Verdejo B, Garcia-Espana E, Basallote MG, Münck E, Que L Jr, Company A, Costas M. J Am Chem Soc. 2015; 137:15833–15842. [PubMed: 26599834]
55. Harman DG, Ramachandran A, Gracanin M, Blanksby SJ. J Org Chem. 2006; 71:7996–8005. [PubMed: 17025286]
56. Luo, Y-R. Comprehensive Handbook of Chemical Bond Energies. Taylor & Francis; Boca Raton: 2007.
57. Kaizer J, Klinker EJ, Oh NY, Rohde JU, Song WJ, Stubna A, Kim J, Münck E, Nam W, Que L Jr. J Am Chem Soc. 2004; 126:472–473. [PubMed: 14719937]
58. Mayer JM. Acc Chem Res. 2011; 44:36–46. [PubMed: 20977224]
59. Biswas AN, Puri M, Meier KK, Oloo WN, Rohde GT, Bominaar EL, Münck E, Que L. J Am Chem Soc. 2015; 137:2428–2431. [PubMed: 25674662]

60. Fujita M, Que L Jr. Adv Synth Catal. 2004; 346:190–194.
61. Van Heuvelen KM, Fiedler AT, Shan X, De Hont RF, Meier KK, Bominaar EL, Münck E, Que JL. Proc Natl Acad Sci USA. 2012; 109:11933–11938. [PubMed: 22786933]
62. Schulz CE, Rutter R, Sage JT, Debrunner PG, Hager LP. Biochemistry. 1984; 23:4743–4754. [PubMed: 6093863]
63. Rittle J, Green MT. Science. 2010; 330:933–937. [PubMed: 21071661]
64. Tiago de Oliveira F, Chanda A, Banerjee D, Shan X, Mondal S, Que L Jr, Bominaar EL, Münck E, Collins TJ. Science. 2007; 315:835–838. [PubMed: 17185561]
65. Roelfes G, Vrajmasu V, Chen K, Ho RYN, Rohde JU, Zondervan C, la Crois RM, Schudde EP, Lutz M, Spek AL, Hage R, Feringa BL, Münck E, Que L Jr. Inorg Chem. 2003; 42:2639–2653. [PubMed: 12691572]
66. Taylor CPS. BBA Protein Struct. 1977; 491:137–148.
67. McGarvey BR. Coord Chem Rev. 1998; 170:75–92.
68. Mas-Ballesté R, Fujita M, Que L Jr. Dalton Trans. 2008:1828–1830. [PubMed: 18369488]
69. Iyer SR, Javadi MM, Feng Y, Hyun MY, Oloo WN, Kim C, Que L Jr. Chem Commun. 2014; 50:13777–13780.
70. Tse CW, Chow TWS, Guo Z, Lee HK, Huang JS, Che CM. Angew Chem Int Ed. 2014; 53:798–803.
71. McGown AJ, Kerber WD, Fujii H, Goldberg DP. J Am Chem Soc. 2009; 131:8040–8048. [PubMed: 19462977]
72. Rittle J, Green MT. Science. 2010; 330:933–937. [PubMed: 21071661]
73. Serrano-Plana J, Aguinaco A, Belda R, Garcia-Espana E, Basallote MG, Company A, Costas M. Angew Chem Int Ed. 2016; 55:6310–6314.
74. Wang Y, Janardanan D, Usharani D, Han K, Que L Jr, Shaik S. ACS Catal. 2013; 3:1334–1341.
75. Sun X, Kryatov SV, Rybak-Akimova EV. Dalton Trans. 2013; 42:4427–4435. [PubMed: 23338901]
76. Padamati SK, Draksharapu A, Unjaroen D, Browne WR. Inorg Chem. 2016; 55:4211–4222. [PubMed: 27074109]
77. Benzaldehyde is also formed in 90 % yield relative to 1a*
78. Makhlynets OV, Das P, Taktak S, Flook M, Mas-Ballesté R, Rybak-Akimova EV, Que L Jr. Chem Eur J. 2009; 15:13171–13180. [PubMed: 19876966]
79. Das P, Que L Jr. Inorg Chem. 2010; 49:9479–9485. [PubMed: 20866083]
80. Kleespies ST, Oloo WN, Mukherjee A, Que L. Inorg Chem. 2015; 54:5053–5064. [PubMed: 25751610]
81. Yan S, Cox DD, Pearce LL, Juarez-Garcia C, Que L Jr, Zhang JH, O'Connor CJ. Inorg Chem. 1989; 28:2507–2509.
82. Kurtz DM Jr. Chem Rev. 1990; 90:585–606.
83. Taktak S, Kryatov SV, Haas TE, Rybak-Akimova EV. J Mol Catal A: Chem. 2006; 259:24–34.

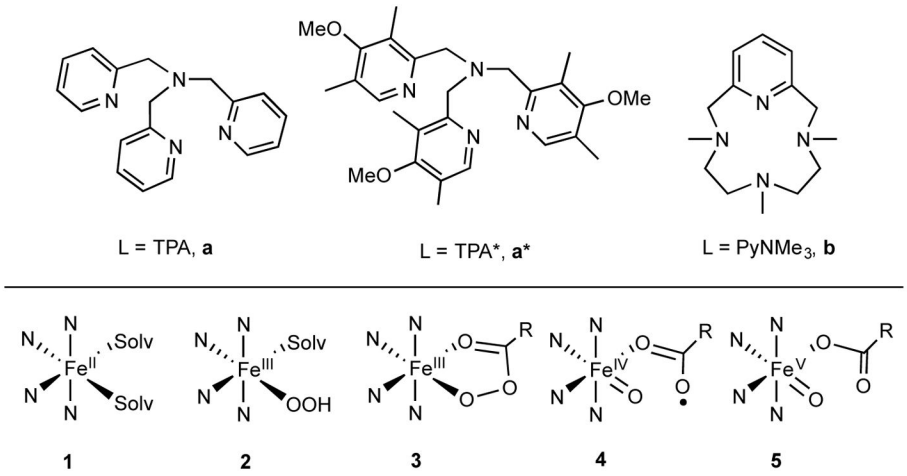

Figure 1.

Top: Ligands used in this study that are proposed to support nonheme $Fe^{V}(O)$ intermediates. Bottom: Various metal species involved in this study. The labelling scheme used throughout the text combines numbers that designate the metal species with letters that designate the ligands. For example, for complexes supported by TPA, the $(L)Fe^{II}$ complex = **1a**, $(L)Fe^{III}$-OOH = **2a**, $(L)Fe^{III}$-OOAc = **3a**, $(L)Fe^{IV}(O)(^{\bullet}OAc)$ = **4a**, and $(L)Fe^{V}(O)(OAc)$ = **5a**.

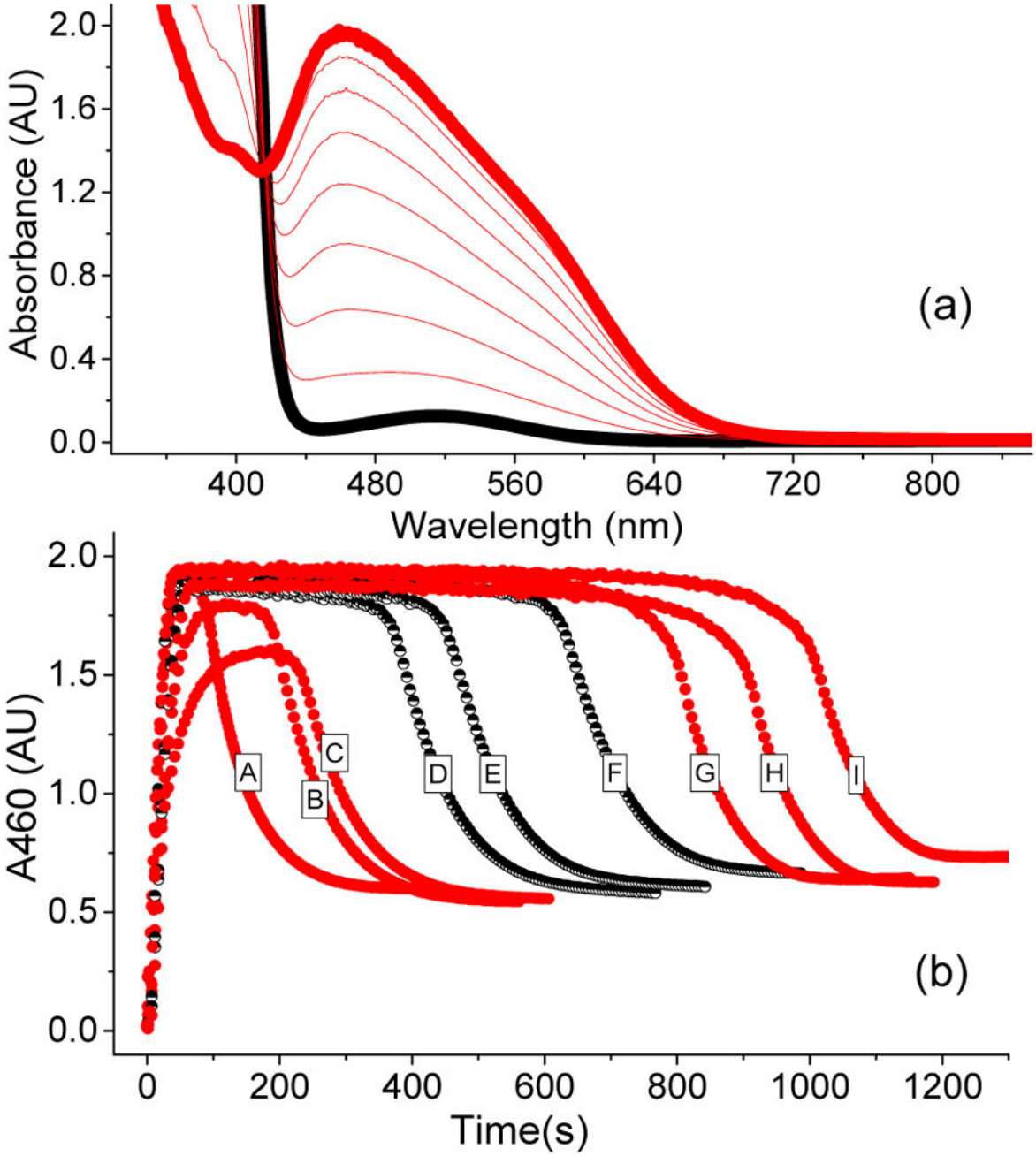

Figure 2.

(a) UV-vis spectrum of a catalytic oxidation reaction involving **1a*** (1 mM), H_2O_2 (10 mM), and AcOH (200 mM) in CH_3CN at −40 °C showing the formation of **3a***, which is generated in 50 % yield relative to the **1a***. (b) The time traces depict the kinetic time course of **3a*** as monitored at 460 nm in the presence of various substrate types and concentrations. A = 250 mM cyclohexadiene; B = 250 mM cyclohexene; C = 250 mM cyclooctene; D = 250 mM 1-octene; E = 125 mM 1-octene; F = 62.5 mM 1-octene; G = 250 mM cyclohexane; H = 250 mM *tert*-butyl acrylate; I = No substrate. The black half-filled circles representing

different 1-octene concentrations demonstrate that the length of the steady state phase is also influenced by this variable.

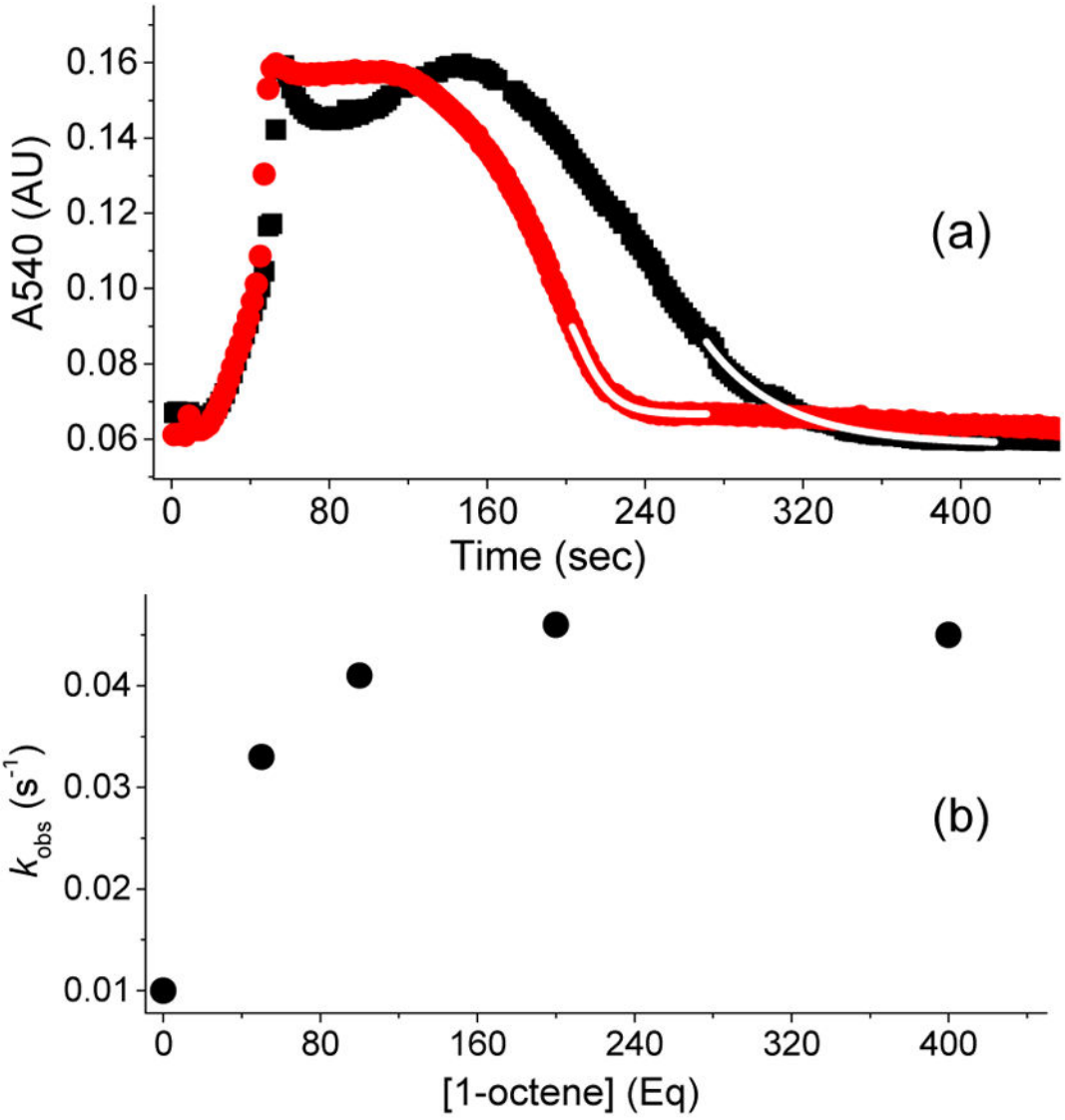

Figure 3.

(a) Kinetic time course of **3a** (monitored at 540 nm), generated in 20 % yield by adding 20 equiv. of H_2O_2 (90 % v/v) to a 0.5 mM solution of **1a** in CH_3CN at −40 °C in the presence of 200 equiv. of AcOH with either no substrate added (black rectangles) or with 50 equiv. 1-octene (red circles). Addition of 1-octene increases the decay rate constant of **3a** by a factor of 5. The fitting to obtain the decay rate constant was conducted during the last turnover (upon depletion of HOOH). The decay time course is exponential as the reaction nears completion. The starting points for the exponential fits shown (white line) are chosen well after the transition from the steady state portion of the time course. (b) Correlation between the observed decay rate constants for **3a** and 1-octene concentration in the catalytic oxidation of 1-octene using **1a** (0.5 mM), H_2O_2 (10 mM), and AcOH (100 mM) in CH_3CN at −40 °C. Note that the kinetic evolution of **3a** was monitored at 540 nm, because the 460 nm λ_{max} has significant background contribution from the decay product due to the low

yield of **3a**. For comparison, the kinetic behavior of 3a* is identical whether followed at its λ_{max} of 460 nm or at 540 nm (Figure S1).

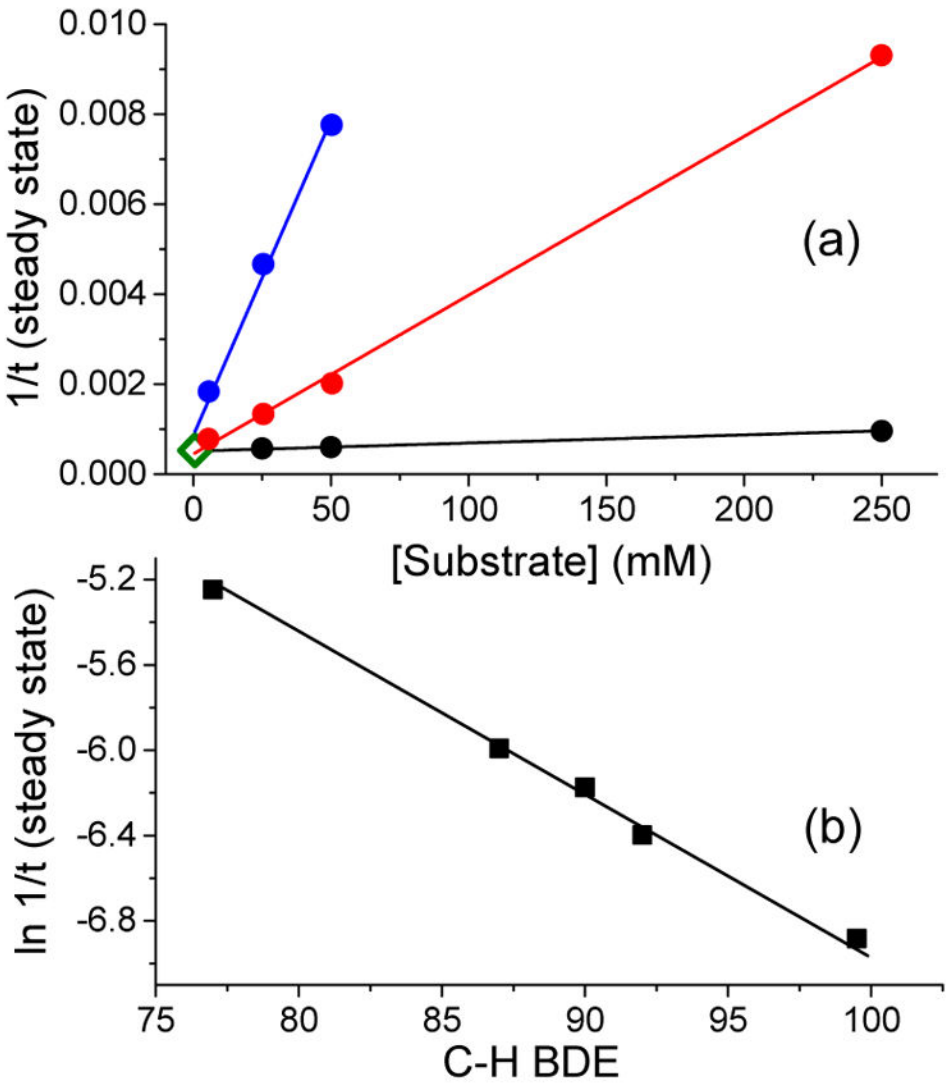

Figure 4.

(a) Plot of the inverse length of the steady state duration of **3a*** (460 nm) as a function of [cyclohexadiene] (blue), [cyclohexene] (red), and [1-octene] (black) in the **1a*** (1 mM)/H_2O_2 (20 mM)/AcOH (200 mM)/substrate mixture in CH_3CN at −40 °C. The point represented by the open diamond at the bottom left corner corresponds to the inverse length of the steady state duration of **3a*** in the absence of any substrate. (b) Correlation between the natural log of the inverse length of the steady state for **3a*** (460 nm) as a function of C–H bond dissociation energy in the **1a*** (1 mM)/H_2O_2 (20 mM)/AcOH (200 mM)/substrate (250 mM) reaction mixture in CH_3CN at −40 °C. Substrates used are from left to right cyclohexadiene, ethylbenzene, toluene, tetrahydrofuran, and cyclohexane.

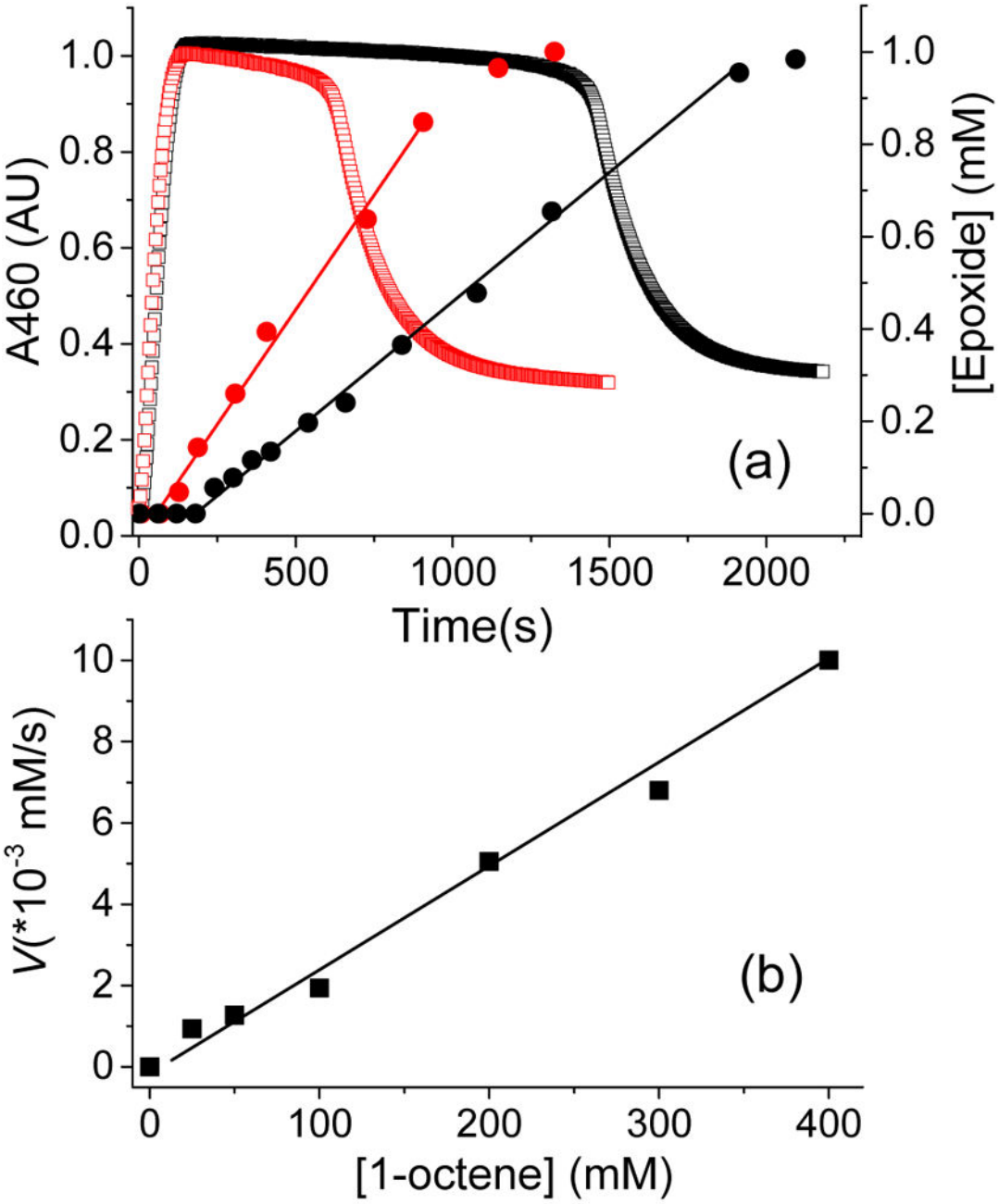

Figure 5.

(a) Monitoring the A460 optical chromophore corresponding to **3a*** (open squares) and the 1,2-epoxyoctane product yields (filled circles) determined by gas chromatography (GC) as a function of time in the **1a***/H_2O_2/AcOH/1-octene reaction at −40 °C, with 100 equiv. (black traces) and 400 equiv. (red traces) of 1-octene. The product formation time traces are fit with a linear function (red and black straight lines) to obtain the rate. **(b)** Plot for the rate of 1,2-epoxyoctane production as a function of [1-octene], in the catalytic oxidation of this substrate using **1a*** (0.5 mM), H_2O_2 (10 mM) and AcOH (100 mM).

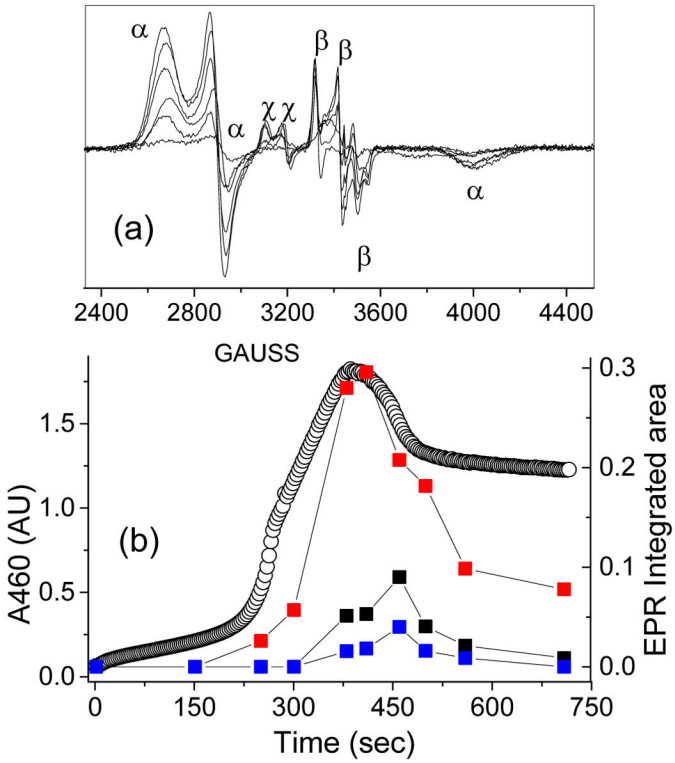

Figure 6.

(a) EPR spectrum of a frozen mixture of **1a*** and AcOOH in CH_3CN showing the formation and decay of **3a*** at g = 2.58, 2.38, 1.73 (α, 28 %), **5a*** at g = 2.07, 2.01, 1.96 (β, 9 %), and **6a*** at g = 2.21, 2.16, 1.94 (χ, 4 %) as a function of time. (b) EPR time-trace for **3a*** (red boxes), **5a*** (black boxes) and **6a*** (blue boxes). The black, open circles represent the optical chromophore of **3a***, monitored at the 460 nm wavelength. EPR conditions: T = 20K, 0.2 mW, 1 mT modulation amplitude.

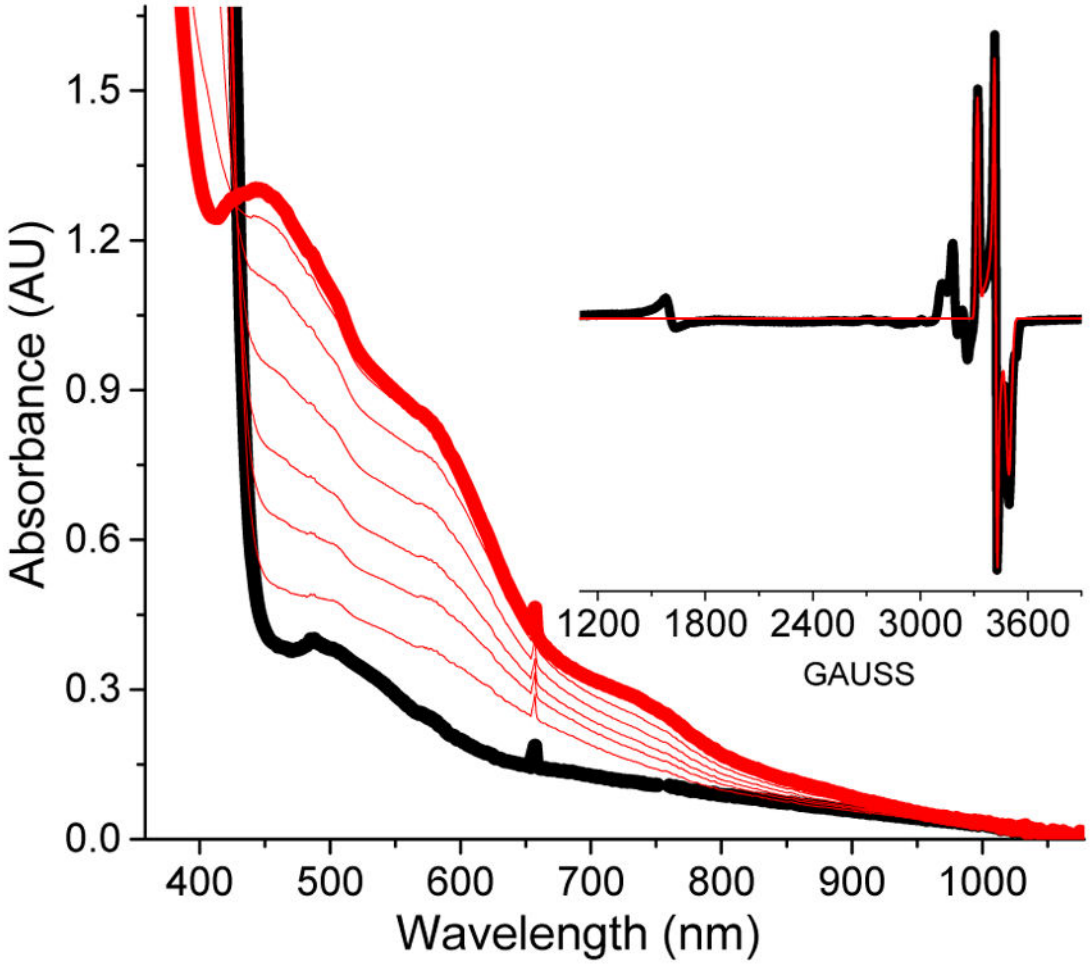

Figure 7.

UV-vis spectral evolution of a reaction of 1.5 mM **1a** with 5 equiv. of cyclohexane peroxycarboxylic acid (CPCA) in $CH_3CN/(CH_3)_2CO$ (1:1 v/v) at −65 °C. (Inset) EPR spectrum of a sample frozen upon maximum accumulation of the chromophoric species. The black trace is the experimental spectrum, while the red trace is the $S = ½$ SpinCount simulation with $g = 2.07$, 2.01, and 1.96 (10 % of total Fe). EPR conditions: T = 20 K, 0.2 mW power, 1 mT modulation.

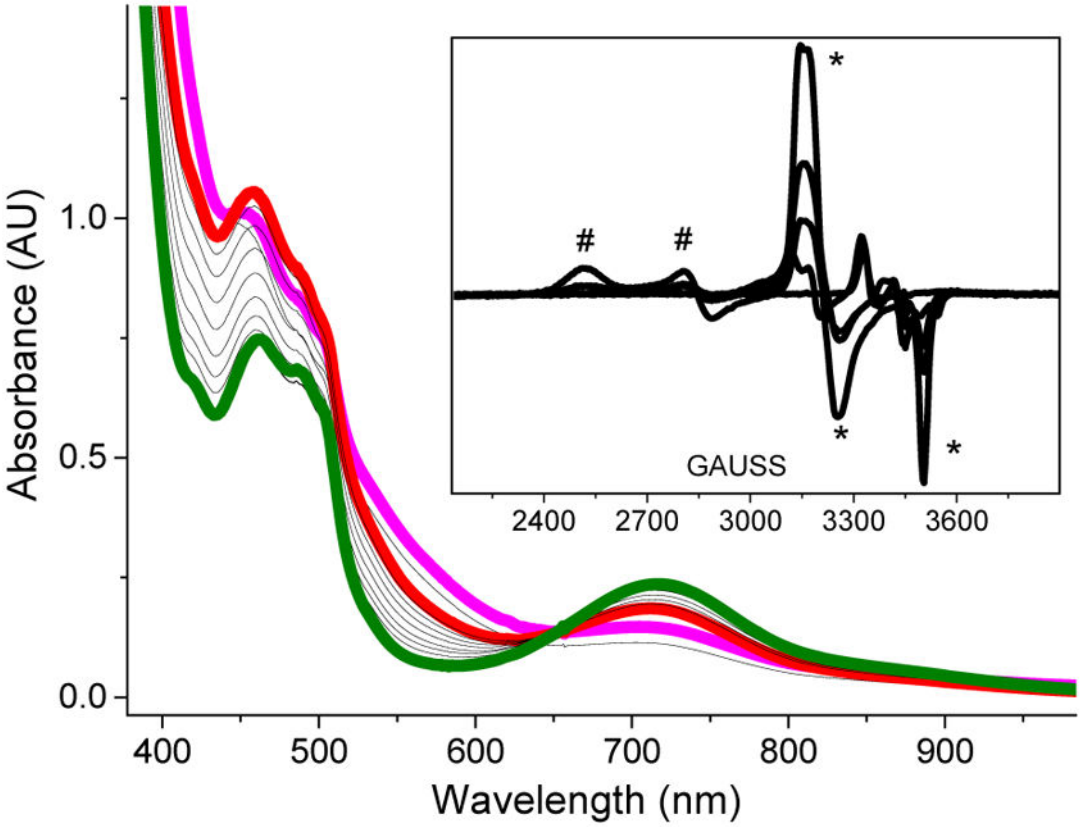

Figure 8.

Addition of 20 equiv. of H_2O_2 to a 1 mM CH_3CN solution of **1a** and AcOH (200 equiv.) at −40 °C, showing (TPA)Fe^{III}–OOAc complex **3a** (red trace), (TPA)Fe^{III}–OOH complex **2a** (purple trace) and (TPA)Fe^{IV}=O (green trace), which derives from the decay of both **2a** and **3a.** Inset: EPR analysis of aliquots of this reaction mixture collected at various time points. EPR signals of **2a** (*) and **3a** (#) can be observed. Both signals are, however, not present at the end of the reaction. EPR conditions: T = 20 K, 0.2 mW, 1 mT modulation amplitude.

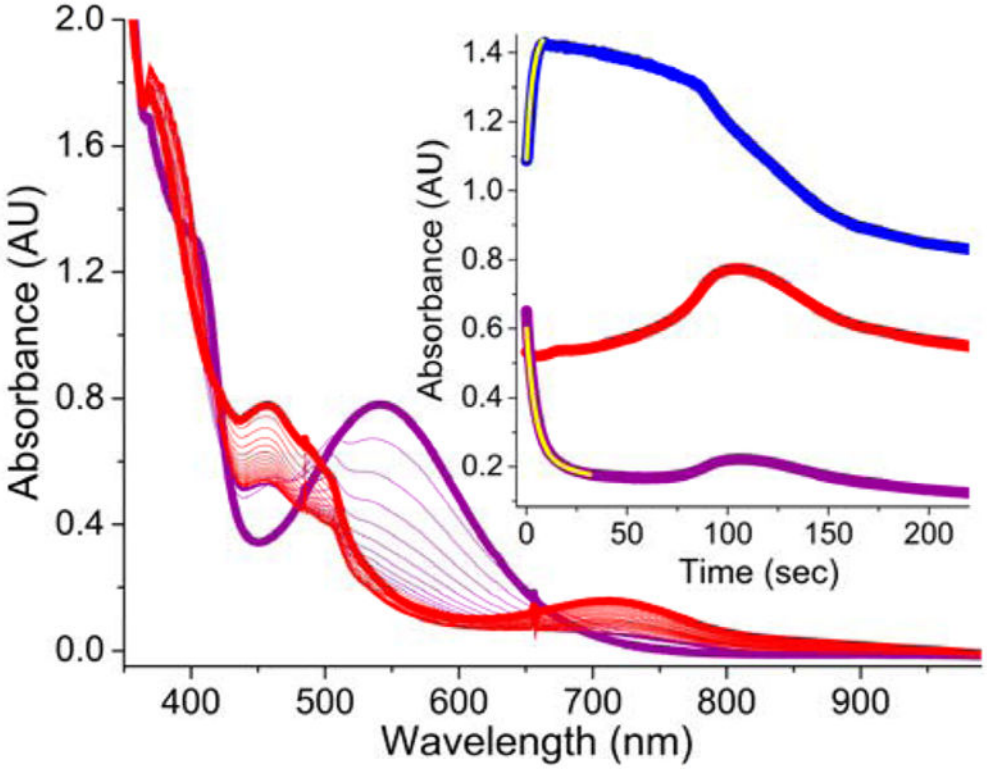

Figure 9.

The addition of AcOH (200 equiv.) to **2a** (CH_3CN, purple trace) generated from a 1 mM CH_3CN solution of **1a** and H_2O_2 (10 equiv.) at −40 °C, initiates the decay of **2a** (purple trace) and the subsequent formation of **3a** (red trace). (Inset) Time trace for the same reaction monitored at 460 nm (red trace), 540 nm (purple trace) and 370 nm (blue trace) wavelengths. The yellow traces in the inset are single exponential fits for the decay of **2a** (k_{obs} = 0.17(1) s^{-1}) and formation of **4a** (k_{obs} = 0.19(1) s^{-1}). While the decay of **2a** is complete within 50 seconds (purple trace), the maximal accumulation of **3a** is not complete until 120 seconds (red trace). **3a** also possesses an electronic absorption band at 540 nm accounting for the increase in absorption at 540 nm concomitant with the increase at its λ_{max} of 460 nm.

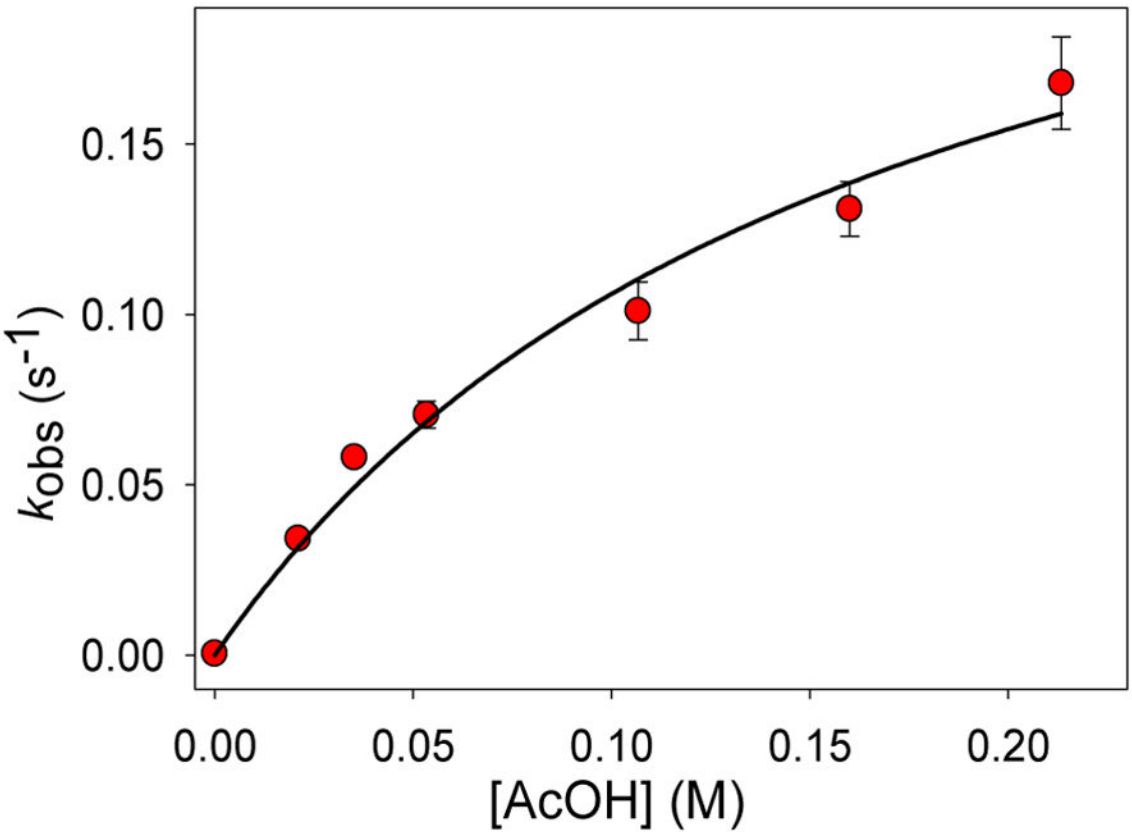

Figure 10.

Decay rate constants of **2a** (λ_{max} = 540 nm) plotted as a function of [AcOH] at −40 °C. The data are fitted with a hyperbolic function. This fit suggests a 2-step process in which fast reversible binding of AcOH (K_d = 0.17 M) is followed by a slower conversion to another species (**4a**) at a maximum apparent rate constant of 0.28 s^{-1}. The maximal rate of decay shows that AcOH increases the decay rate of **2a** by ~ 900-fold when saturation is achieved.

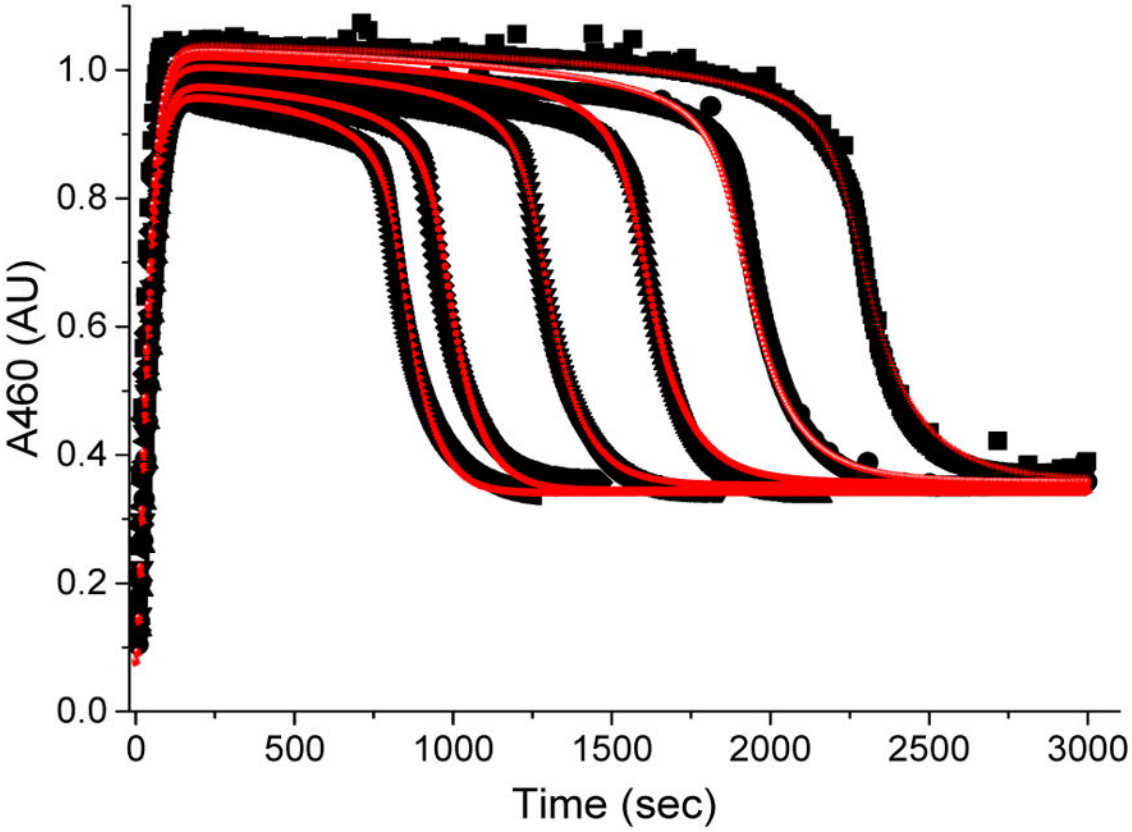

Figure 11.

Black traces represent kinetic time courses of **3a*** (460 nm) generated by adding 20 equiv. of H_2O_2 (90 % v/v) to a 0.5 mM solution of **1a*** in CH_3CN −40 °C in the presence of 200 equiv. of AcOH and various equivalents of 1-octene. The red traces indicate fits derived from numerical simulation of the experimental data according to the model presented in Scheme 2. The traces from right to left correspond to 0, 50, 100, 200, 400 and 600 equiv. of 1-octene added.

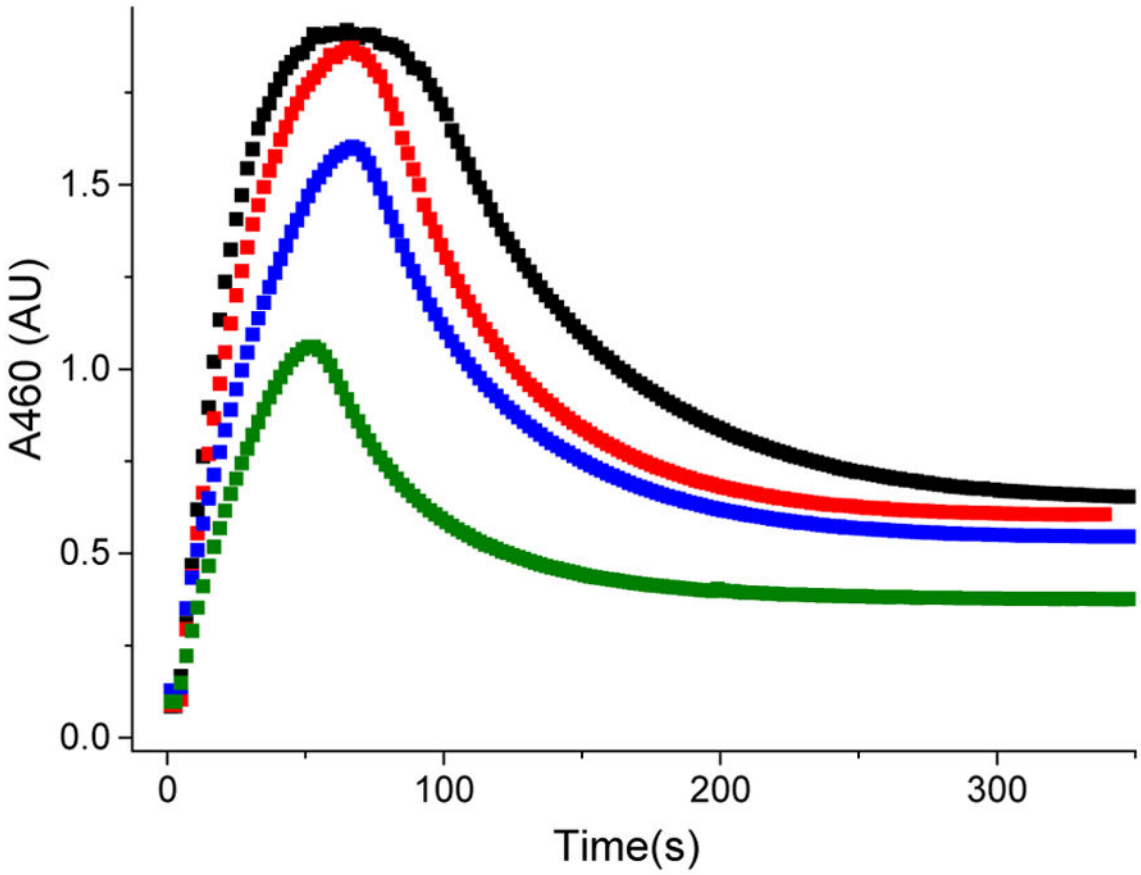

Figure 12.

Kinetic trace for the formation and decay of **3a*** in the reaction between **1a*** and H_2O_2 (10 equiv.) in the presence of AcOH (200 equiv.) and 50 (black), 150 (red), 500 (blue), and 1000 (green) equivalents of 1,4-cyclohexadiene, demonstrating that the maximum yield of **3a*** depends on the amount of 1,4-cyclohexadiene present in solution.

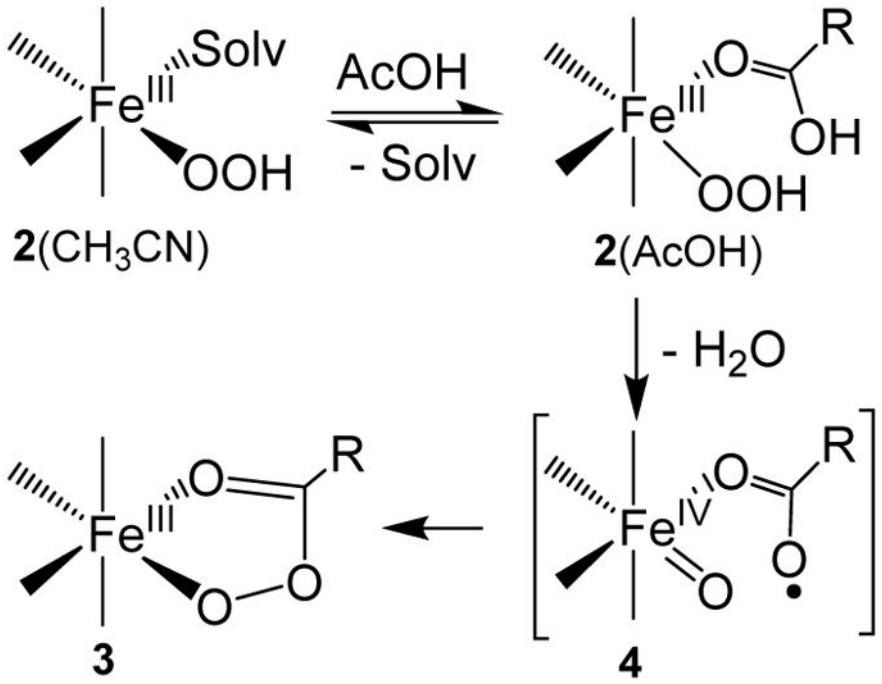

Scheme 1.

Proposed mechanism for the formation of the $S = ½$ Fe^{III}–OOAc intermediate based on previous DFT calculations.[44, 45, 48, 74]

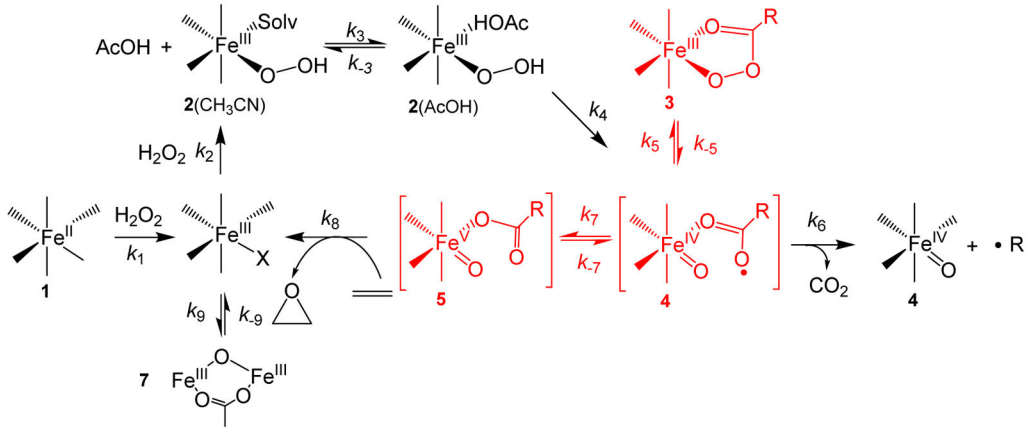

Scheme 2.

Chemical model used to fit the kinetic evolution of **3a*** (460 nm) as a function of 1-octene concentration shown in Figure 11. The unique equilibrium among the components of the catalytic troika, **3**, **4** and **5**, is highlighted with red. The H/D KIE observed in the reaction of **2** with AcOH (Table 2) would be connected in the k_4 step in this scheme.

Table 1

EPR properties of the $S = ½$ iron species previously observed in reaction mixtures of nonheme iron catalysts with H_2O_2/RCOOH or peracids

Precursor	Oxidant (Temp)	High *g*-anisotropy (*g*2.7) species % spin	Low *g*-anisotropy (*g*2.07) species (*2.07, 2.01, 1.96*) % spin	ref
(TPA)Fe^{II}	H_2O_2/AcOH (−40 °C) or mCPBA (−60°C)	*2.74, 2.42, 1.53* 4 – 21%	not observed	44, 50, 54
(TPA*)Fe^{II}	H_2O_2/AcOH or mCPBA (−40 °C)	*2.58, 2.38, 1.73* 43 – 50 %	not observed	50
[(TPA*)Fe^{III}]$_2$O	H_2O_2/AcOH (−85 °C)	*2.58, 2.38, 1.73* observed but % not reported	2 – 3 %	51
(BPMEN)Fe^{II}	H_2O_2/AcOH (−70 °C) or peracids (−60 °C)	*2.69, 2.42, 1.70* 4–10 %	not observed	50
(*S,S*-PDP)Fe^{II}	H_2O_2/AcOH (−70 °C) H_2O_2/2-EhOH (−70 °C)	*2.66, 2.42, 1.71* 2 – 3 % not observed	not observed 2 – 3 %	40, 52 53
(*S,S*-PDP*)Fe^{II}	H_2O_2/AcOH (−40 to −85 °C)	*2.72, 2.42, ?* 7%	not observed	48
[(*S,S*-PDP*)Fe^{III}]$_2$O	H_2O_2/AcOH or AcOOH (−65 to −85 °C)	*2.52, 2.41, 1.80* observed but % not reported	<2 %	51, 53
($PyNMe_3$)Fe^{II}	AcOOH (−40 °C)	not observed	40 %	54

Abbreviations used: BPMCN = *N,N′*-dimethyl-*N,N′*-bis(2-pyridylmethyl)-*trans*-1,2-diaminocyclohexane; BPMEN = *N,N′*-dimethyl-*N,N′*-bis(2-pyridylmethyl)ethane-1,2-diamine; mCPBA = *meta*-chloroperbenzoic acid; PDP = *N,N′*-bis(2-pyridylmethyl)-2,2′-bipyrrolidine; PDP* = *N,N′*-bis(3,5-dimethyl-4-methoxy-2-pyridylmethyl)-2,2′-bipyrrolidine; $PyNMe_3$ = 3,6,9-trimethyl-3,6,9-triaza-1(2,6)-pyridinacyclodecaphane; 2-EhOH = 2-ethylhexanoic acid; TPA = tris(2-pyridylmethyl)amine; TPA* = tris(3,5-dimethyl-4-methoxy-2-pyridylmethyl)amine.

Table 2

Eyring activation parameters and KIE values for the decay of peroxoiron(III) intermediates and product formation rates in catalytic oxidation reactions by iron(II) complexes.

Reaction mixture	Chemical step monitored	$\Delta H^{\ddagger}$ kJ/mol	$\Delta S^{\ddagger}$ J/mol•K	KIE[a]	ref
(TPA)Fe^{II} + H_2O_2 in CH_3CN/H_2O + 1-octene	H_2O-accelerated decay of (TPA)Fe^{III}-OOH (**2a**)	45(1)	−95(10)	2.5	[28]
	Product formation	47(1)[b]	-	2.5	[28]
(TPA)Fe^{III}–OOH in CH_3CN + AcOH	AcOH-accelerated decay of (TPA)Fe^{III}-OOH (**2a)**	25(2)	−151(10)	1.7	This work
(TPA*)Fe^{II} + H_2O_2 in CH_3CN/AcOH + 1-octene	(TPA*)Fe^{III}–OOAc (**3a***) decay	74(1)	45(10)	1.0	This work
	Product formation	54(2)[b]	-	1.0	

[a] Determination of KIE values involved reactions conducted with 200 equiv. of added H_2O vs D_2O or AcOH vs AcOD.

[b] These values correspond to the activation energies obtained by Arrhenius analysis.

Table 3

EPR properties of $S = ½$ iron species related to the high-valent iron intermediates.

Complex [a]	**EPR $g_{x,y,z}$**	**^{57}Fe A_x, A_y, A_z (MHz)**	**% Fe**	**ref**
(N4Py)Fe^{III}–OOH	2.16, 2.11, 1.98	− 9, − 53, + 6	100 %	65
(TPA*)Fe^{III}–OOAc (**3a***)	2.58, 2.38, 1.72	− 62, + 26, + 42	50 %	50
(TPA)Fe^{III}–OOAc (**3a**)	2.74, 2.43, 1.52	–	23 %	*b*
6a*	2.22, 2.16, 1.94	A_x = 60	4 %	51/*b*
6a	2.21, 2.16, 1.96	A_x = 60	5 %	*b*
5a*	2.07, 2.01, 1.96	A_y = 65	9 %	51/*b*
5a	2.07, 2.01, 1.96	A_y = 65	10 %	*b*
[($PyNMe_3$)Fe^{V}(O)]$^{3+}$ (**5b**)	2.07, 2.01, 1.96	$A_x \ll A_y = 47 \gg A_z$	40 %	54
[(TMC)Fe^{V}(O)(NC(O)Me)]$^{+}$	2.05, 2.01, 1.97	−47, −17, 0	50 %	61
[(TAML)Fe^{V}(O)]$^{−}$	1.99, 1.97. 1.74	−67, −2, − 22	95 %	64
[(Me_3TACN)Fe^{IV}(O)(Cl-acac$^{•+}$)]$^{2+}$	1.97, 1.93, 1.91	–	35 %	70
[($TBP_8Cz^{•+}$)Fe^{IV}(O)]	2.09, 2.05, 2.02	–		71
HRP-Cpd I	1.99 (broad)	− 26, − 26, − 8		62
CPO-Cpd I	1.72, 1.61, 2.00	− 42, − 41, − 3		72
CYP119-Cpd I	2.00, 1.96, 1.86	− 38, − 44, − 4		72

[a] Abbreviations used: CPO = chloroperoxidase; CYP119 = cytochrome P-450; HRP = horseradish peroxidase; Me_3TACN = 1,4,7-trimethyl-1,4,7-triazacyclononane, Cl-acac = 3-chloro-acetylacetonate; N4Py = bis(2-pyridylmethyl)-bis(2-pyridyl)methylamine; $PyNMe_3$ = 3,6,9-trimethyl-3,6,9-triaza-1(2,6)-pyridinacyclodecaphane; TAML = tetraamidate macrocyclic ligand; TBP_8Cz = octakis(4-tert-butylphenyl)corrolazine; TMC = tetramethylcyclam, TPA* = tris(3,5-dimethyl-4-methoxypyridyl-2-methyl)amine.

[b] This work.

Table 4

Rate constants obtained from the simulation of the time trace of 3a* (460 nm) in the presence of varying amounts of 1-octene at −40 °C.

Rate constants	Best fit	Lower bound[a]	Upper bound[a]	Experimentally measured	ref
k_1 (M^{-1} s^{-1})	7.6	5.5	14	12 for $(PyNMe_3)Fe^{II}$ at −35 °C 35 for $(BPMEN)Fe^{II}$ at 20 °C 82 for (*S,S*-PDP)Fe^{II} at 20 °C	54 48 48
k_{-1} (s^{-1})	0	0	0	0	
k_2 (M^{-1} s^{-1})	640	507	800		
k_{-2} (s^{-1})	0	0	0.1		
k_3 (M^{-1} s^{-1})	11	9	920		
k_{-3} (s^{-1})	0	0	0.1		
k_4 (s^{-1})	0.137	0.128	0.16	0.28 for **2a**	
k_{-4} (s^{-1})	0	0	0.0090	0	
k_5 (s^{-1})	0.057	0.050	0.058		
k_{-5} (s^{-1})	0.016	0.015	0.017	0.01 for **3a***	
k_6 (s^{-1})	0.047	0.045	0.047		
k_{-6} (s^{-1})	0.0	0.0	0.0	0	
k_7 (s^{-1})	0.28	0.27	0.29		
k_{-7} (s^{-1})	0.45	0.41	0.52		
k_8 (M^{-1} s^{-1})	0.77	0.70	0.92	0.032 at −85 °C (~ 0.77 at −40 °C)[b]	
k_{-8} (s^{-1})	0.0	0.0	0.0		
k_9 (s^{-1})	0.012	0.0090	0.015		
k_{-9} (s^{-1})	0.0	0.0	0.00060		

[a]The lower and upper bounds for each rate constant depict the ranges in which each fitted parameter can vary independently while still allowing an acceptably good fit. Note that the rate constant k_3 is not constrained by the data as a large variation in its value can fit the available data.

[b]This extrapolation was made, assuming a 2-fold acceleration in the rate constant for every 10-degree rise in temperature.